ORIGINAL ARTICLE

Microstructure, mechanical and tribological properties of AA5083-TiO2 nanocomposite by multi-pass friction stir processing

Panagiotis Karmiris-Obratański[1,2] · Ioannis G. Papantoniou[2,3] · Beata Leszczyńska-Madej[4]

Abstract

This study examines the impact of Friction Stir Processing (FSP) with TiO_2 nanoparticle incorporation on the microstructural, mechanical, and tribological properties of AA5083 Metal Matrix Composites (MMCs). It offers a detailed analysis of the alterations in the alloy's characteristics due to FSP. Microstructural examination was conducted using optical microscopy (OM) and scanning electron microscopy (SEM). Significant findings include the microstructural refinement where TiO_2 nanoparticle addition during FSP shrank the grain size from 20 to 3 μm after one pass, which then rose to 7 μm following four passes. Mechanical properties, specifically microhardness and tensile strength, were assessed. Results indicated that after four FSP passes, the material can reach a yield strength of 192 MPa and an ultimate tensile strength (UTS) of 359 MPa, alongside a consistent microhardness of 103 HV0.1. Furthermore, it was observed that increasing FSP passes enhances energy absorption, although it remains lower than that of the base material. Analysis of fracture and wear mechanisms has led to the conclusion that with more passes, fracture mechanisms transition to a mix of ductile and brittle behaviors, and the friction coefficient decreases by up to 22.95%.

Keywords Friction stir processing · Microstructure · Wear · Mechanical properties · Fracture behavior

1 Introduction

Particle-reinforced metal matrix composites (MMCs) have garnered significant attention across industries such as automotive, aerospace, and defense due to their exceptional properties [1]. By incorporating particles into metal matrices, MMCs offer heightened elastic modulus, stiffness, and wear resistance, making them indispensable for demanding applications [2]. This innovation allows engineers to tailor material properties to specific requirements, resulting in weight savings [3], increased temperature resistance [4], and improved fatigue and corrosion resistance [5]. Despite challenges in manufacturing, MMCs stand as a promising solution to elevate the performance and durability of critical components in various high-performance sectors [6]. At a specific concentration level, the potential for enhancing strengthening mechanisms [7] becomes notably pronounced through the incorporation of smaller particles, especially within the nano-sized range [8]. However, in contrast to composites reinforced with micro-sized particles, the fabrication of nanocomposites poses significant complexities. These challenges primarily arise due to the intricate nature of achieving a consistent and homogeneous dispersion of nano-sized reinforcements within metallic substrates [9]. Traditional methodologies such as powder metallurgy and liquid processing, encounter limitations in effectively addressing the intricate spatial and interfacial considerations intrinsic to the dispersion of nano-particulates within the matrix [10].

Friction stir processing (FSP) has emerged as a compelling and innovative approach within the realm of fabricating

✉ Panagiotis Karmiris-Obratański
  karmiris@agh.edu.pl

1 Advanced Manufacturing Laboratory, Department of Manufacturing Systems, Faculty of Mechanical Engineering and Robotics, AGH University of Krakow, Kracow, Poland

2 School of Mechanical Engineering - Laboratory of Manufacturing Technology, National Technical University of Athens, Athens, Greece

3 Department of Naval Architecture, School of Engineering, University of West Attica, 12243 Egaleo, Greece

4 Department of Materials Science and Non-Ferrous Metals Engineering, Faculty of Non-Ferrous Metals, AGH University of Krakow, 30-059, Cracow, Poland

MMCs [11]. Rooted in the fundamental tenets of Friction Stir Welding (FSW) [12], FSP involves the intricate manipulation of materials. In FSP and FSW, a rotating tool endowed with distinct components, including a pin and a shoulder, is meticulously introduced into the material designated for fusion [13]. This tool is meticulously translated along the trajectory of the joint, thus orchestrating the intricate process [14]. The process involves inducing localized heating in the immediate vicinity of the pin, engendering a region of controlled material softening [15]. This thermal softening, coupled with the synergistic interaction of simultaneous tool rotation and translation, engenders a concerted material flow mechanism from the fore of the pin to its aft. FSP falls under the classification of Severe Plastic Deformation (SPD) techniques [16]. SPD methods encompass various procedures that deliberately subject materials to high levels of plastic deformation, inducing significant changes in their microstructure without invoking traditional melting and recrystallization processes [17]. solid-state nature of the process and its potential to facilitate metallurgical bonding without the need for molten phase intermediates. FSP is usually used for modification of the microstructure like crystallographic grain refinement, distribution of particles and morphology [18].

Many authors have studied the improvements of hardness, ductility, plasticity, yield strength, and strength by FSP. Several researchers selected pure metal powder reinforcement to the aluminum matrix serves to attain aluminum matrix composites. This has led to the exploration of alloying elements like Fe [19], Ni [20], and Mo [21], which are incorporated into the aluminum matrix to achieve aluminum matrix composites distinguished by exceptional interface bonding. However, due to the nature of FSP, some powders tend to create intermetallic structures, that reduce the plasticity and enables the crack propagation [22]. On the other hand, some researchers incorporate ceramic particulates, particularly those composed of Silicon Carbide (SiC) [23] and Aluminum Oxide (Al_2O_3) [24], are frequently favored as reinforcements in aluminum matrix composites due to their distinctive material characteristics. These encompass elevated hardness, a notably high melting point, substantial elastic modulus, and exceptional thermal stability at elevated temperatures [25]. These properties collectively position ceramic particles as highly suitable additives for augmenting the mechanical and thermal properties of the resulting composite materials. Research on ceramic particle-reinforced aluminum matrix composites consistently shows that adding ceramic particles significantly improves the matrix's strength and wear resistance. Derazkola H. et al. [26] conducted processing and characterization endeavors on nanocomposites consisting of polycarbonate and alumina (PC/Al_2O_3). Employing an innovative approach, they harnessed the additive powder Fed FSP technique, facilitated by a novel tool configuration, to facilitate the dispersion of nanoparticles within the base metal matrix. Their conclusions underscored that PC/Al_2O_3 additive nanocomposites, comprising an 8% weight fraction, produced via the FSP technique, exhibited exceptional microstructural integrity marked by the absence of defects, alongside significant advancements in mechanical properties, notably a substantial enhancement in tensile strength by approximately 26%. A novel hybrid aluminum MMC was developed by Mija et al. [27] by adding MoS_2 and CeO_2 particles. The authors by analyzing the wear behaviur and corrosion resistance found that, manufactured MMC using lower processing speeds and multiple passes exhibited reduced friction coefficients and minimal wear losses as well. In addition, the composites produced with a feed rate of 30 mm/min and 1 pass have better corrosion resistance, but with 2 passes and the same feed rate the MMC exhibited better wear resistance and microhardness. The study discussed in [28] introduces a potential method for manufacturing an AA5083 foam MMC strengthened with nano-γAl_2O_3 utilizing the FSP technique. The findings show that the post the foaming process, the γ-Al_2O_3 nanoparticles were predominantly distributed in intercellular locations in a heterogeneous manner. Using the same nanoparticles, Orłowska et al. [29] investigated the manufacturing of coarse and ultrafine MMC using FSP. The authors observed that after one FSP pass, the nanoparticles formed non-uniform agglomerations, which reduced the mechanical properties compared to the base material. However, after two FSP passes, there was a slight increase in Ultimate Tensile Strength (UTS), along with improvements in elongation and yield strength. In their study, Ostovan et al. [30] utilized multi-pass FSP to embed Carbon Nanotubes (CNTs) and Fe_2O_3 nanoparticles into an AA5083 matrix. The results demonstrated significant improvements in the mechanical properties of the MMC. Specifically, after five FSP passes, the MMC exhibited enhancements by factors of 1.6, 2.7, 3.5, and 3.1 in hardness, Yield Strength (YS), UTS, and wear resistance, respectively, when compared to the BM. Li et al. [31] conducted an examination focused on the feasibility of producing a carbon nanotube-reinforced aluminum matrix composite (CNT Al MMC) and nano-Al_4C_3 MMC through the utilization of FSP. In essence, the study accomplished the successful creation of high-strength, highly ductile in situ synthesized nano-Al_4C_3/Al composites through FSP applied to CNT/Al composite. At a rotation rate of 800 rpm, the Al_4C_3/Al composite displayed a 1.6-fold increase in elongation compared to CNT/Al composites, with a retained yield strength of 95%. Ata et al. [32] investigated the microstructural and mechanical attributes of a novel hybrid material, AA1050/Ni-Cu-Fe, synthesized through a combination of mechanical alloying and FSP. The main findings show that an instance of 80% Ag-coated Ni, the peak values of ultimate tensile strength and

elongation were observed, registering at 100 MPa and 10%, respectively. In the optimal scenario, the failure mechanism exhibited ductile characteristics, attributed to the motion of dislocations and plastic deformation. The impact of multi-passes FSP conpined with SiC and TiB_2 in the mechanical and metallurgical properties was investigated by Chittoriya et al. [33]. The authors found that nanoparticles enchased the UTS [34] and facilitated large plastic deformation through precipitation and dislocation strengthening [35]. Finally, Zhang et al. [36] investigated the effect of FSP underscore the complex interplay of grain boundary dynamics and textural changes resulting from FSP, which influence the microstructural and potentially mechanical properties of Al6061. The authors found a 50% grain size refinement and the proportion of low-angle grain boundaries increased to 22.3%, suggesting incomplete recrystallization during the FSP.

Building on insights from previous research, this study investigates the production of AA5083 MMCs reinforced with TiO_2 nanoparticles through a multi-pass FSP approach. The main objective is to explore how the number of FSP passes affects the integration of nanoparticles and their impact on the microstructural characteristics, mechanical properties, and wear resistance of the composites. Specifically, the study seeks to delineate the relationship between multi-pass FSP technology, TiO_2 and the structural, microstructural, and both macroscopic and microscopic properties of the materials. This research includes comprehensive evaluations using microhardness tests, tribological assessments, and tensile strength measurements. Microscopy techniques such as OM, Focus Variation Microscopy (FVM), and Scanning Electron Microscopy (SEM) equipped with Electron Backscatter Diffraction (EBSD) and Energy Dispersive Spectroscopy (EDS) are utilized for detailed analysis of grain size and chemical composition. This approach allows for a deeper understanding of the underlying mechanisms. Distinct from previous works, this study uniquely focuses on the combined effects of multiple FSP passes and nanoparticle reinforcement, offering novel insights into optimizing the properties of MMCs.

2 Materials and methods

2.1 Materials

The microstructure of AA5083, an aluminum-magnesium alloy, embodies a critical determinant of its mechanical characteristics and performance attributes. This intricate microstructural framework comprises an aluminum matrix punctuated by a heterogeneous arrangement of precipitate phases [37]. These phases are formed as a consequence of the alloy's composition and thermal history, exhibiting varying morphologies, sizes, and distribution patterns [38]. The chemical composition of the 6 mm plates AA5083-H111 is presented in the Table 1. Recognized as a non-heat treatable aluminum alloy, AA5083 is prominently employed across sectors encompassing transportation, marine, and chemical industries. Its salient attributes encompass commendable corrosion resistance within seawater-laden atmospheres, coupled with a heightened formability exhibited particularly under conditions marked by lower temper states [39]. This specific alloy demonstrates notable mechanical attributes, featuring a tensile strength that reaches as high as 260 MPa, a yield strength spanning from 270 to 345 MPa, and a hardness ranging between 95 and 100 HV. The chemical composition of the investigated alloy was analyzed using a FOUNDRY-MASTER Xpert spectrometer. The Table 1 represent the mean values obtained from three independent measurements. In addition, the used plates had initial dimensions of $200 \times 300 \times 5$ mm.

The experimental investigation involving AA5083 MMC was conducted through the implementation of FSP, which was executed utilizing a custom-modified milling machine. A visual representation of the friction stir process as well as the tool dimensions can be observed in Fig. 1. The FSP tool employed in these trials was crafted from heat-treated tool steel, characterized by a flat shoulder with a diameter of 22 mm, and a pin component possessing a cylindrical configuration with a diameter of 4 mm and a height of 5 mm, featuring a right-handed thread. The operational parameters encompassed a rotational speed (Vrot) of 1000 rpm in conjunction with a transverse speed (Vt) of 13 mm/min, thereby orchestrating the fundamental dynamics of the process.

To facilitate the preparation of the MMC, a groove was meticulously created with precise dimensions, featuring a width of 1 mm and a depth of 2 mm. The grove was filled with TiO_2 nano-powder with average particle dimension of 220 nm.

2.2 Methods

2.2.1 Microstructural characterization

The microstructural assessment of both the fabricated MMC and the raw material entails the examination of the cross-sectional specimen surface. The specimens preparation

Table 1 Chemical composition of AA 5083, wt%

Mg	Mn	Fe	Si	Cu	Zn	Cr	Ti	Al
4.5	0.7	0.4	0.2	0.1	0.05	0.2	0.11	Bal

Fig. 1 Graphical representation of the FSP Process, tool and groove dimensions
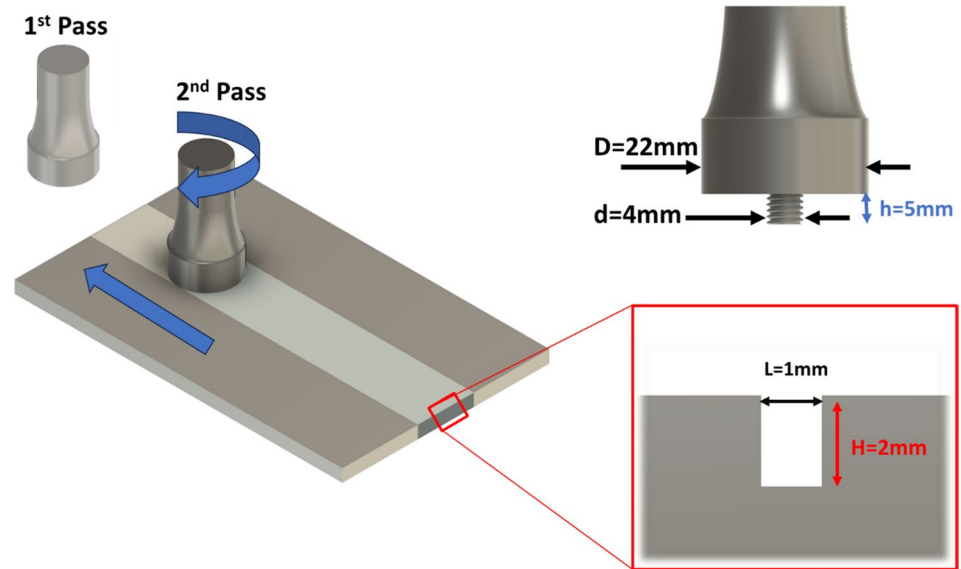
was conducted a Wire Electrical Discharge Machining (WEDM), specifically Neospark B500 (Knuth, Germany). The specimens where inducted, prepared and polish for the metallographic investigation. The examination of the sample's microstructure, both before and after FSP, involved employing Olympus GX51 optical microscopy and Hitachi SU-70 Scanning Electron Microscopy (SEM). In addition, Electron Back Scattered Diffraction (EBSD) was utilized to analyze grain size and orientation, while EDS analysis was conducted to determine the chemical composition at micro-scale regions.

Analyses using the electron backscatter diffraction (EBSD) method were performed using a Hitachi S-3400N scanning electron microscope and detector with dedicated software made by HKL company. An accelerating voltage of 20 kV was used for the tests. The sample was tilted at an angle of 70° at a distance of approximately 20 mm from the column. Electron backscatter diffraction analysis was performed to obtain maps of the crystal lattice orientation distribution on the surface of the test sample with a 0.15 μm step at a magnification of 2000x. The colors of the solved orientations were assigned according to the basic IPF triangle notation. The results are presented in the form of a map of the crystallographic orientation distribution on the sample surface. The texture results were also calculated for the orientation intensity to both PF and IPF with $10 \times 10°$ clustering.

2.2.2 Tensile test

For a better understanding of the mechanical properties of the MMC, for a more comprehensive grasp of the mechanical properties of the MMC, testing was conducted on specimens extracted along the direction of the tool's feeding rate during FSP. To obtain specimens for the tensile test, a WEDM process is employed in a direction perpendicular to that of the FSP. To ensure the accuracy of the results, the tensile specimens were prepared in accordance with ASTM D618-14, using Type IV dimensions, and each experiment was repeated three times. The experiments were conducted using a universal testing machine (Instron 4482) under room temperature and ambient air conditions, with a consistent strain rate of 7×10^{-4} s^{-1}. Stress–strain curves were constructed based on the load—displacement data obtained. These curves were then utilized to calculate the energy absorbed until failure and to establish the yield strength. The values reported herein represent the average results obtained from three separate and independent experiments.

2.2.3 Microhardness characterization.

This subsection establishes the correlation between the material's microstructure, its microhardness characteristics, and the influence of the number of FSP passes. The analysis involved studying the microhardness distribution in the test specimens and relating it to microstructural observations. An automated DuraScan 80 G5 machine by Struers was employed to assess microhardness distribution patterns. The testing procedure involved applying a measuring force, which lasted between 2 and 8 s, and then maintaining the test force for 10 to 15 s after removing the force. The diagonal lengths of the indentations were measured, and their arithmetic mean was computed. In accordance with EN ISO 14577–1:2005, each specimen underwent 90 indentations with a load of 0.1 kgf. These indentations were arranged in 6 rows, each containing 15 measurements, and the distance between each measurement point was 0.2 mm. It was

determined that the microhardness of the 5083 aluminum alloy substrate is approximately 85 $HV_{0.1}$.

2.2.4 Tribological performance evaluation.

The tribological performance assessment of the as-received aluminum alloy and compared with the FSP samples involves a block in ring T-05 tribotester. The tests were performed at a room temperature in dry friction with a constant load of 57N and a sliding distance of 250 and 1000 m at a speed of 1.3 m/s following the ASTM G 77 standard and each wear test was performed 3 times. A block of 20×4x4mm was used as a wear specimen carefully and a specimen of 100 Cr6 bearing steel, which had undergone heat treatment and possessed a hardness level of 55 HRC, was employed as a counter sample with a diameter measuring 49.5 mm.

3 Results and discussion

3.1 Microstructure characterization

The parameters of the FSP process have a crucial influence on the quality of the microstructure produced. The studies presented in this paper show that the structure of the FSP zone changes with an increase in the number of FSP passes.

A distinctive attribute of the resulting microstructure is the arrangement of the material, forming a pattern resembling 'onion rings'. The structure of these rings is characterized by a repetitive pattern, which is a result of a periodic change in the distribution of the titanium dioxide reinforcing component. As elucidated by R. S. Mishra in his publication [40], these patterns repeat at intervals corresponding to the linear distance covered by the tool during each revolution. This phenomenon is potentially linked to the oscillations of the tool's rotational axis around its linear axis of movement. Findings from Hamilton et al., as detailed in references [41], suggest that the emergence of regions with varied precipitate densities relates to the non-uniform distribution of temperatures within the FSP zone. This nonuniformity leads to the creation of material layers with differing temperatures [42]. Notably, the most heterogeneous microstructure is manifested in the composite generated through a single FSP pass, displaying areas (bands) largely devoid of the reinforcing phase. The introduction of multiple FSP passes results in a considerable homogenization of the microstructure, accompanied by the near disappearance of the characteristic onion ring pattern (Figs. 2, 3, 4).

An equally typical feature of the fabricated composites is the fully recrystallized, equiaxial, fine grain SZ mixing zone, which is formed by intense plastic deformation at elevated temperatures (Fig. 3). Many examples of grain refinement as a result of FSP modification are cited in works presented by Ma [43], Węglowski [44] and Heidarzadeh [45], but there are still no sufficiently developed models that correlate tool geometry and process parameters with the final grain size observed in the material after FSP treatment. No aggregation of nanometric particles of the reinforcing phase was observed in the microstructure, which is a characteristic feature of conventionally manufactured composite materials, as nanoparticles tend to form clusters. In addition to the uniform distribution of TiO_2 reinforcing phase particles in the microstructure, the Cr, Mn and Fe-rich precipitates present in the alloy were fragmented (Figs. 4, 5, and 6).

The obtained results of the EBSD analysis present a noteworthy microstructure refinement in alloy 5083 following the incorporation of TiO_2 particles during the friction stir modification process (Figs. 7, 8, 9). Prior to the FSP treatment, the initial grain size measured around 20 μm. After a single FSP pass with the introduction of TiO_2, the average matrix grain size is reduced to approximately 3 μm. However, with an increase to 4 FSP passes, the grain size enlarges, averaging around 7 μm. In the context of electron backscatter diffraction (EBSD) analysis, the base alloy sample lacking TiO_2 exhibits predominant directions along the <101> and <112> poles, with a maximum texture intensity of 1.85. Misorientation angle measurements reveal a prevalence of larger angles beyond 15°, accounting for 57.7% of the measured population. Conversely, for the sample subjected to 1 FSP pass with TiO_2, EBSD analysis indicates an ascendance of orientations around the <111> and <110> poles, accompanied by a heightened texture intensity of 2.19. The misorientation angle measurements disclose a significant dominance of angles surpassing 15°, constituting nearly 95% of the examined population. These orientations are organized in a prominent circular arrangement. Subsequent tests on a specimen after 4 FSP passes highlight the predominance of the texture component <110>, with a maximum intensity of 2.86. Notably, a comparable trend emerges with the prevalence of large misorientation angles, encompassing almost 82% of the scrutinized population.

As can be seen from the above figures (Figs. 2, 3, 4, 5, 6, 7, 8, 9), the addition of TiO_2 nanoparticles and the employment of multi-pass FSP processing have a significant influence on the microstructure refinement. According to research, utilizing SPD and dynamic recrystallization (DRX) through the stirring action of a rotating tool may refine the grain structure of an aluminum alloy [46]. Furthermore, researchers have found that pinning effect of hard nanoparticles of Al_3Ti and MgO, with a size of around 50 nm, can further refine the grain structure [15]. During the DRX, these particles accelerate nucleation through the mechanism of Particulate Stimulation Nucleation (PSN), which restricts the rate of grain boundary migration through Zener pinning
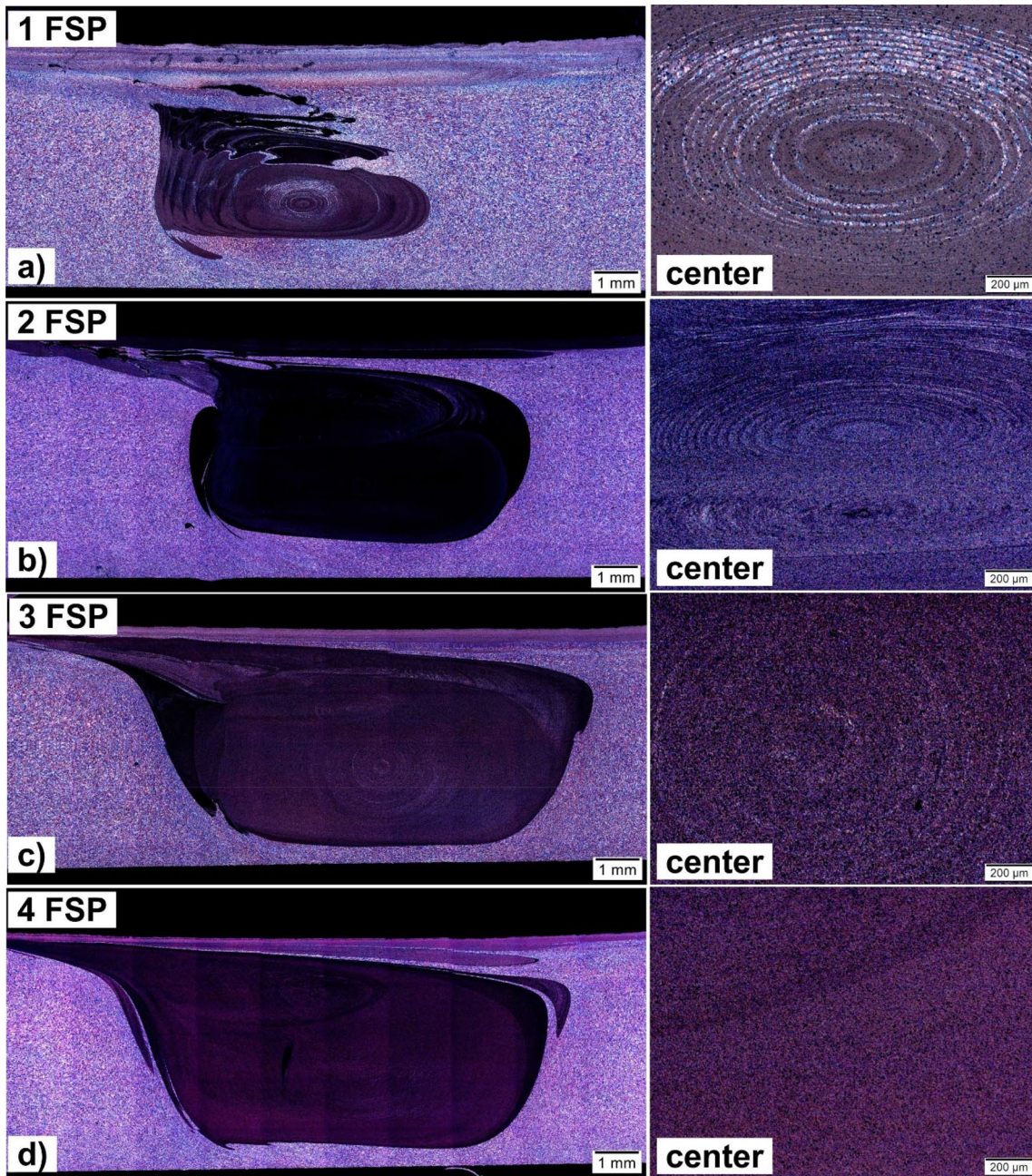
Fig. 2 Microstructure of AA 5083 – TiO$_2$ after FSP with visible unmodified area (left side); photo on the right shows the center of modified area: **a** 1 FSP, **b** 2 FSP, **c** 3 FSP, **d** 4 FSP; LM

mechanism [47]. The following table shows the effect of multi-pass FSP with the addition of TiO$_2$ nanoparticles on the misorientation angles.
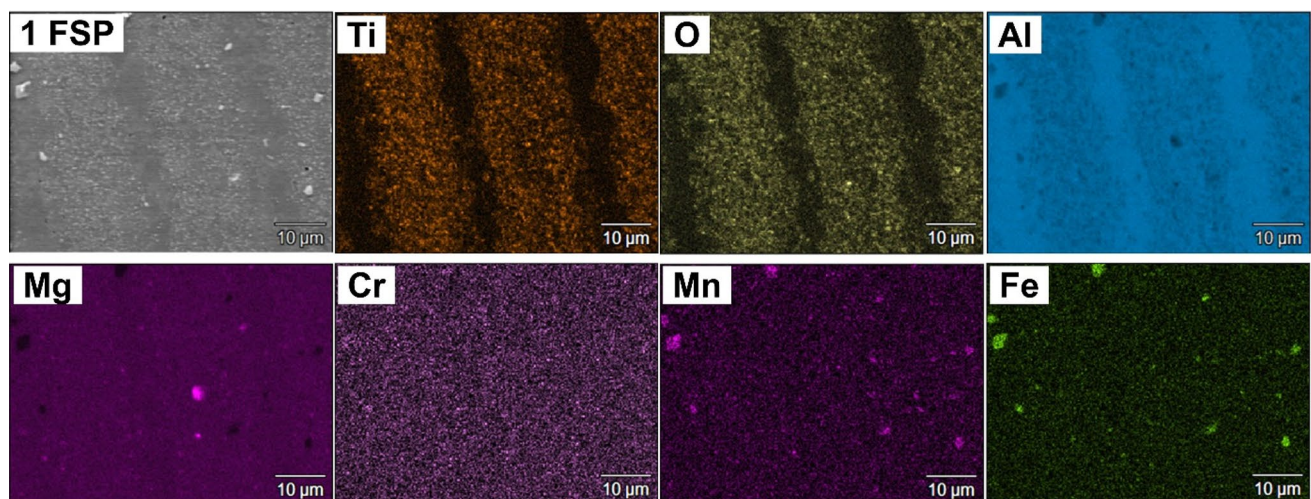
3.2 Mechanical properties.

The mechanical properties of AA5083 MMCs reinforced with TiO$_2$ nanoparticles, fabricated through multi-pass FSP, were comprehensively characterized through tensile testing.

This section presents the results and analysis of the mechanical behavior, including yield stress and ultimate tensile strength, and energy absorption along with maximum strain, in relation to the number of FSP passes. More analytically, Fig. 10 illustrates the stress—strain behavior for specimens with different number of FSP pass where Fig. 11 presents plots illustrating the energy absorption until failure, yield stress, ultimate tensile strength and maximum strain values for a better evaluation and interpretation of the results. These
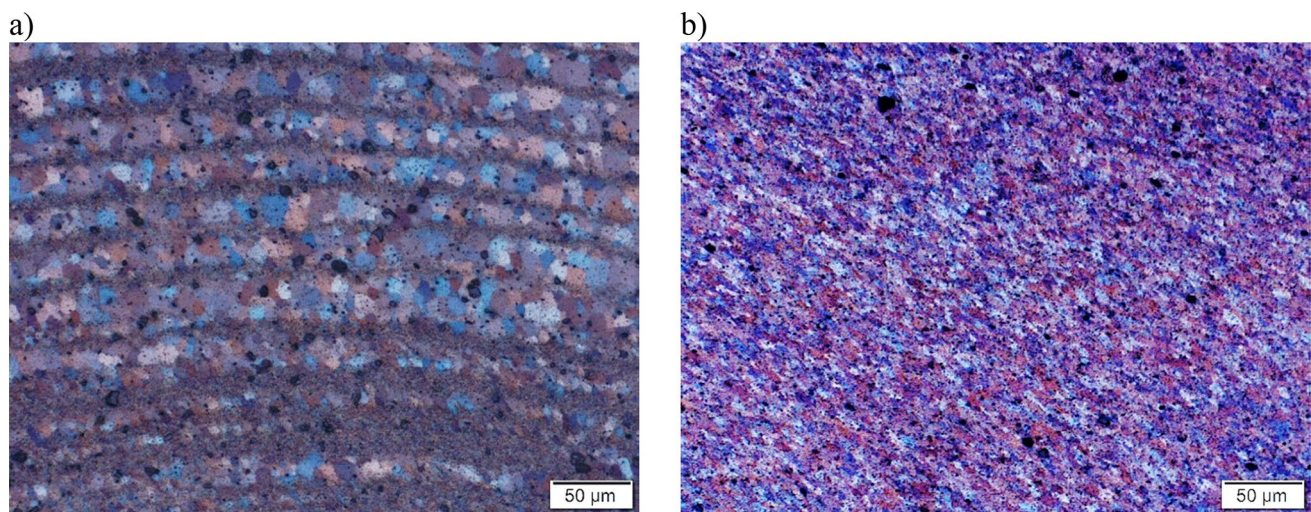
Fig. 3 Microstructure of AA 5083 – TiO$_2$ after FSP; **a** 1FSP, **b** 3FSP; recrystallized grains are visible in the photo

Fig. 4 Microstructure and elemental distribution maps: Ti, O, Al, Mg, Cr, Mn and Fe; 1 FSP

plots allow for a clear comparison and analysis of the relationship between FSP passes and the resulting mechanical properties.

3.2.1 Yield stress and ultimate tensile strength

Yield stress and UTS are critical mechanical properties that provide insights into the material's resistance to deformation and its maximum strength before fracture, respectively. These properties were closely examined in relation to the number of FSP passes. Initially, we should mention that the yield strength and the UTS of the base material were measured 142 MPa and 322 MPa, respectively. For the reinforced specimens, as illustrated in Fig. 10a, b, the results highest mean yield stress observed was 192 MPa (values ranging

from 187 to 198), and it was achieved in the reinforced specimen subjected to 4 FSP passes. Concurrently, the reinforced specimens subjected to 4 FSP passes exhibited the highest mean ultimate tensile strength of 359 MPa (values ranging from 344 to 372). Furthermore, we can observe that we have a linear increase of the mean values with respect to the increase of the FSP passes. These results emphasize the substantial strengthening effect imparted by the FSP process and the introduction of the nanoparticles in the aluminum matrix, indicating increased resistance to plastic deformation and improved overall strength.

The remarkable increase in both yield stress and UTS (specifically for the 3&4-pass specimens) can be attributed to several factors resulting from multiple FSP passes. One key factor is the improved dispersion of nanoparticles
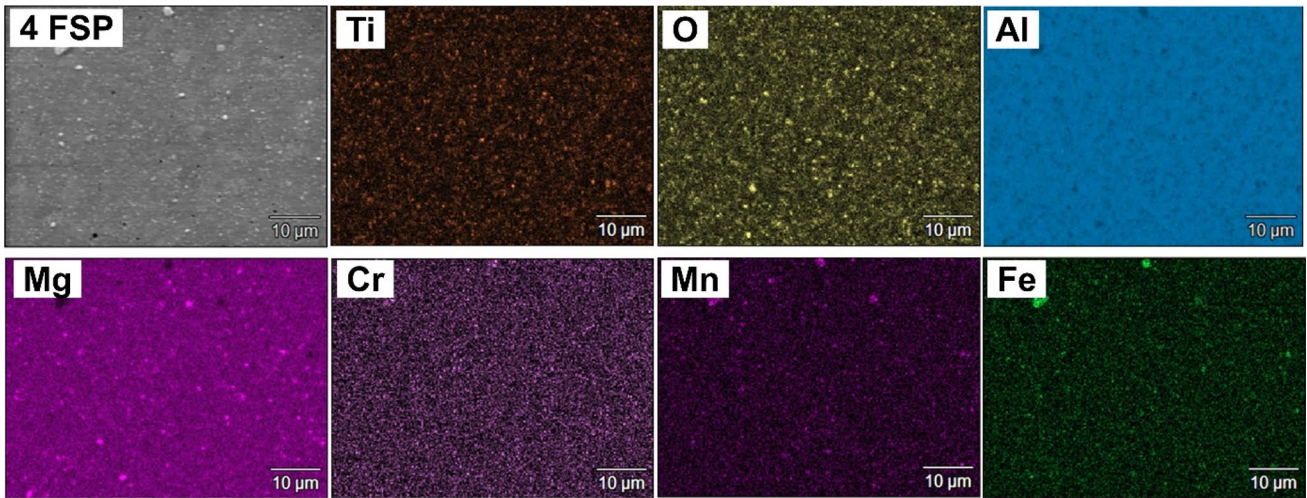
Fig. 5 Microstructure and elemental distribution maps: Ti, O, Al, Mg, Cr, Mn, and Fe; 4 FSP
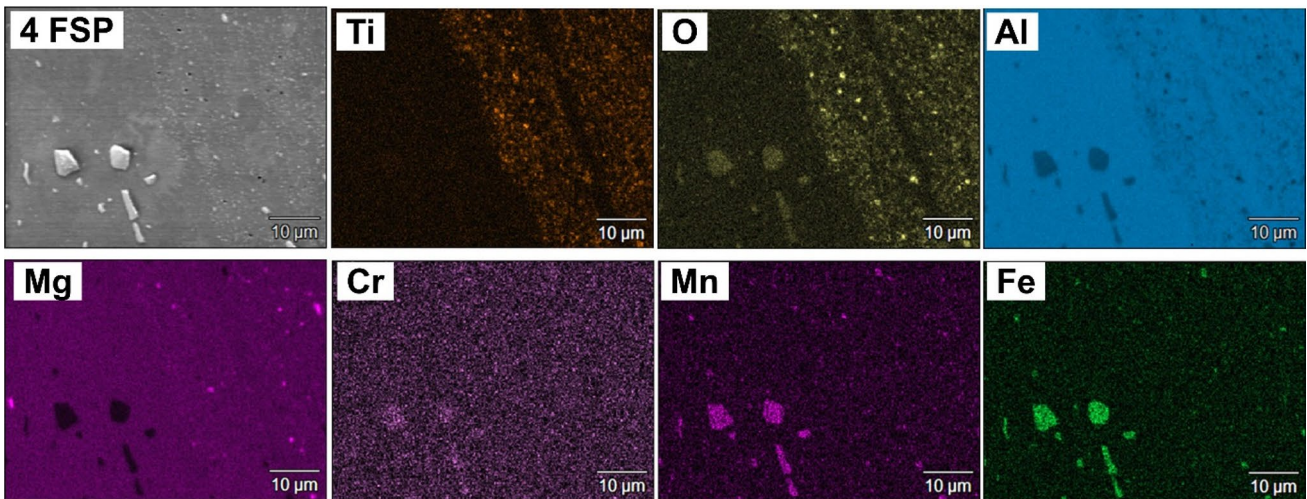

Fig. 6 Microstructure and elemental distribution maps: Ti, O, Al, Mg, Cr, Mn, and Fe; transition zone, 4 FSP
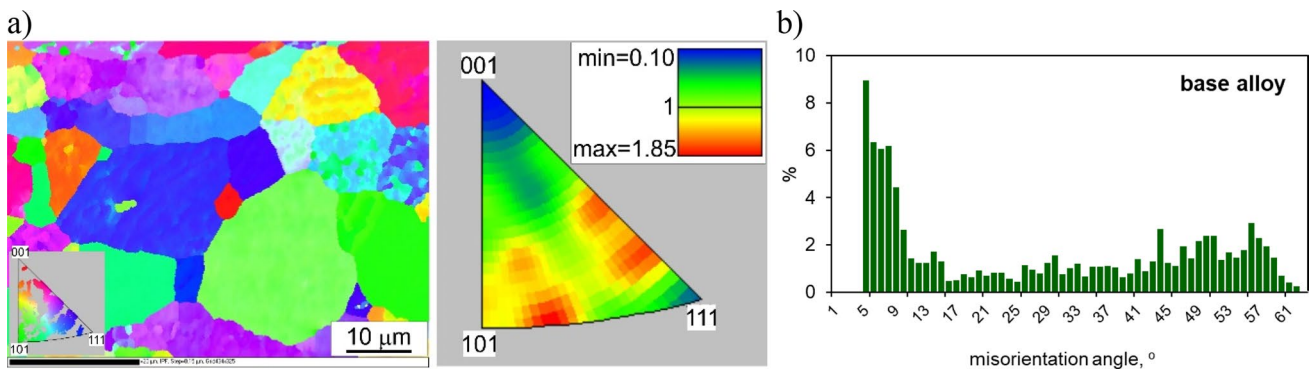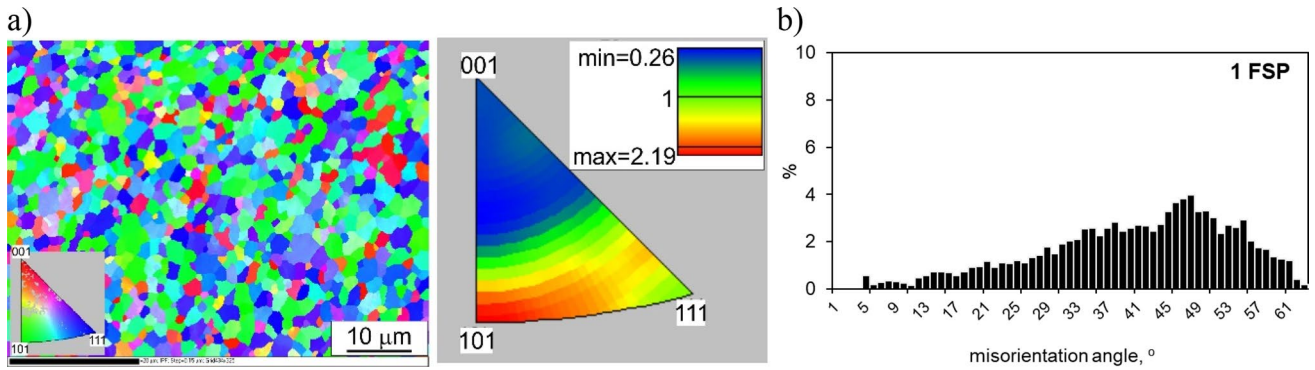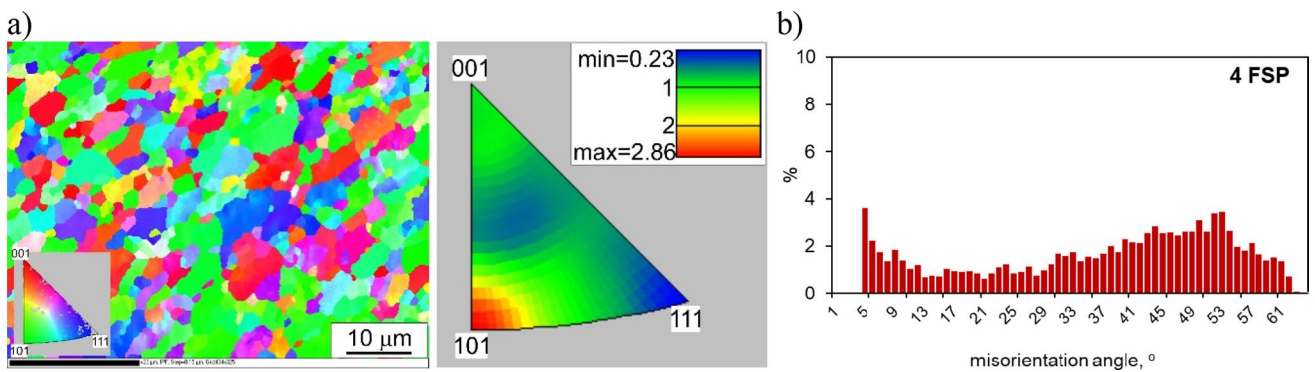

Fig. 7 Results of the EBSD analysis of the base alloy without TiO_2 particles; **a** EBSD maps showing changes in orientation and a basic triangle—orientation intensity, **b** changes in disorientation angles

Fig. 8 EBSD analysis results of the base alloy with TiO_2 particles – 1 FSP; **a** EBSD maps showing changes in orientation and a basic triangle—orientation intensity, **b** changes in disorientation angles

Fig. 9 Results of the EBSD analysis of the base alloy with TiO_2 particles – 4 FSP; **a** EBSD maps showing changes in orientation and a basic triangle—orientation intensity, **b** changes in disorientation angles

Fig. 10 Stress–strain diagrams obtained from tensile testing
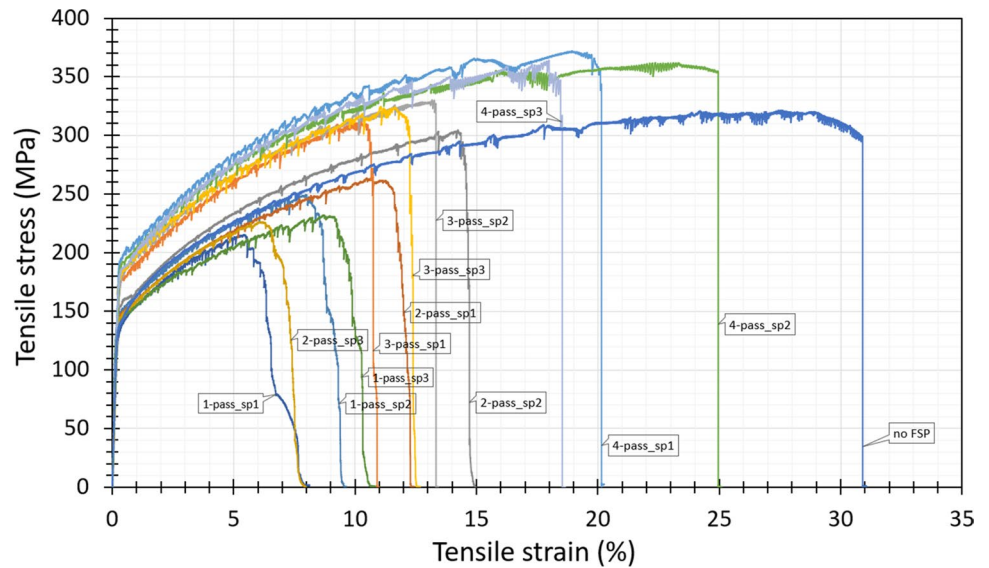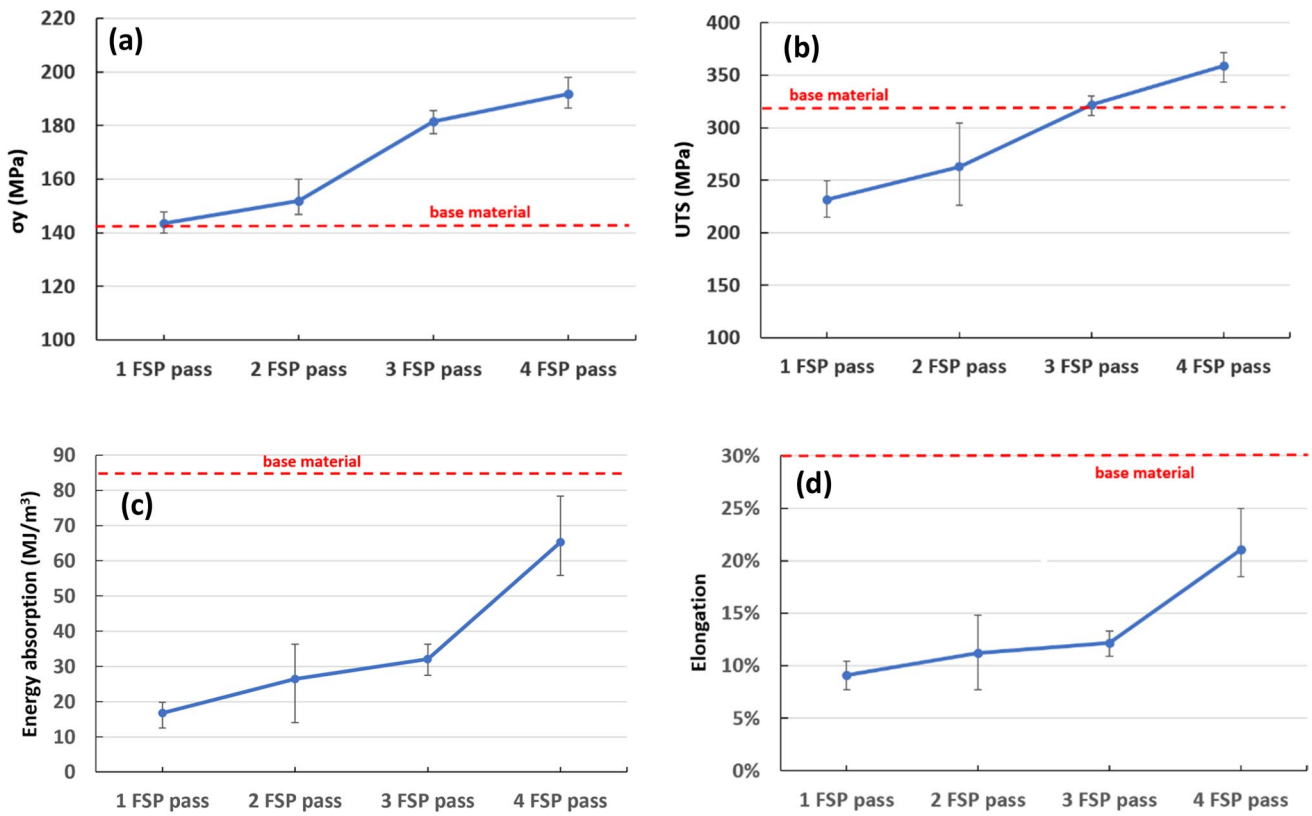
Fig. 11 Impact of varying FSP passes on **a** the yield strength, **b** the UTS, **c** the tensile energy absorption and **d** the maximum elongation

within the metal matrix. During the FSP process, as the rotating tool passes through the material multiple times, it promotes the uniform distribution of nanoparticles, preventing agglomeration. This enhanced dispersion ensures that the strengthening effects of the nanoparticles are more uniformly realized throughout the material. Furthermore, the multiple FSP passes lead to a refined microstructure characterized by smaller grains and the absence of particle agglomerates. The smaller grain size (along with the presence of the nanoparticles) contributes to increased material strength, as it hinders the propagation of dislocations and provides additional strengthening mechanisms. In addition, the absence of particle agglomerates eliminates potential stress concentration points, further enhancing the material's resistance to deformation and fracture.

Upon a detailed examination of the tensile curves, it becomes evident that the introduction of TiO_2 nanoparticles leads to dynamic strain aging [48]. This effect is linked to the reduced magnesium content in the aluminum lattice, a consequence of the formation of MgO particles upon adding TiO_2 as it can be seen in figs. 4, 5. It is important to note that the indented yielding phenomenon, typically observed in these scenarios, is attributed to the presence of magnesium atoms in the alloy [49]. Numerous studies, referenced as [50], have investigated the impact of varying concentrations

of TiO_2 on mechanical properties. The findings indicate that as the concentration of TiO_2 is increased, there is a degradation in mechanical properties [59]. This deterioration is attributed to the non-uniform distribution of TiO_2 and the presence of un-reacted nanoparticles, which are believed to hasten the formation of micro-voids within the material. This phenomenon of a lower UTS and elongation can be also observed in case of the samples that underwent 1 and 2 FSP passes due to due to this non-uniform dispersion of nanoparticles (see Fig. 3, 4).

3.2.2 Energy absorption and maximum strain

Energy absorption and maximum strain at failure are essential parameters that collectively characterize the material's ability to dissipate energy during deformation and its extent of deformation before fracturing.

Notably, the sample without FSP passes (base material) demonstrated the highest energy absorption, recording a value of 85 MJ/m^3. This exceptional energy-absorbing capability can be attributed to the absence of structural modifications induced by FSP. However, for the reinforced specimens as the number of FSP passes increased, a gradual enhancement in energy absorption was observed (Fig. 11c), reaching its zenith at four FSP passes with values ranging

from 56 to 79 MJ/m^3 and a mean value of 66 MJ/m^3. The increase in energy absorption with FSP passes can be attributed to improved material consolidation and the formation of a refined microstructure, enhancing the material's capacity to absorb energy before fracture.

Regarding maximum strain, the results followed the energy absorption values. As illustrated in Fig. 11d, the base material exhibited the highest value, indicating greater ductility. In contrast, the sample subjected to four FSP passes displayed a lower maximum strain due to its higher stiffness. This result underscores the trade-off between strength and ductility in MMCs and highlights the importance of selecting the appropriate FSP parameters to achieve the desired balance between these properties.

3.3 Microhardness distribution

In the Fig. 12 below, it depicts the microhardness distribution of the cross-section of FSPed specimens. Each sample comprises three parallel rows, each containing 20 microhardness tests. Contrary to other studies [51], as the number of passes increases, the microhardness decreases [52]. The average microhardness measurements along the SZ revealed values of 137 HV$_{0.1}$ for a single-pass FSP, 120 HV$_{0.1}$ for a two-pass FSP, 111 HV$_{0.1}$ for a three-pass FSP, and 103 HV$_{0.1}$ for a four-pass FSP, respectively, although the microhardness of the base materials is close to 80HV$_{0.1}$ with a standard deviation of 5HV$_{0.1}$ [42]. The main reasons for the hardness improvement are as follows: a) the refinement of grain structure [53], b) the heightened dislocation density

[54], and c) the amalgamation of rigid TiO$_2$ particles within the aluminum matrix as it can be seen in Fig. 2 and the MMC's surface area similarly to the study of Girish and Anandakrishnan [55].

The observed increase in microhardness during the first pass can be causally linked to several influential factors. These include the notable reduction in grain size, as substantiated by the findings from the EBSD analysis (refer to Figs. 6, 7, 8). Furthermore, the close proximity of TiO$_2$ nanoparticles situated between grains, as evidenced in Fig. 3a, contributes significantly to this phenomenon. In addition, the compact and well-integrated structure of the MMC surface area, as illustrated in Fig. 2, further reinforces the enhanced microhardness. With each successive FSPed pass, several notable changes can be observed. First, the MMC surface area undergoes expansion, as evident from the increased coverage. Second, there is a discernible growth in grain size attributed to the phenomenon of heat-induced recrystallization [56], which can be corroborated by comparing Fig. 8 and Fig. 9. Third, the size of nanoparticles undergoes reduction, and they exhibit improved dispersion throughout the material and plays significant role in the grain boundary pinning [57]. The cumulative effects of these factors lead to a more uniform microhardness in the material. This implies that the interplay between the TiO$_2$ nanoparticle concentration, its distribution (Fig. 2), and the resultant microstructural changes which can be attributed to the interfacial reactions, the creation of hard MgO and Al$_3$Ti nanophases, and the thermal stability of the grain structure in the SZ [50], contributes positively to the uniformity in microhardness.

Fig. 12 Microhardness distribution test results
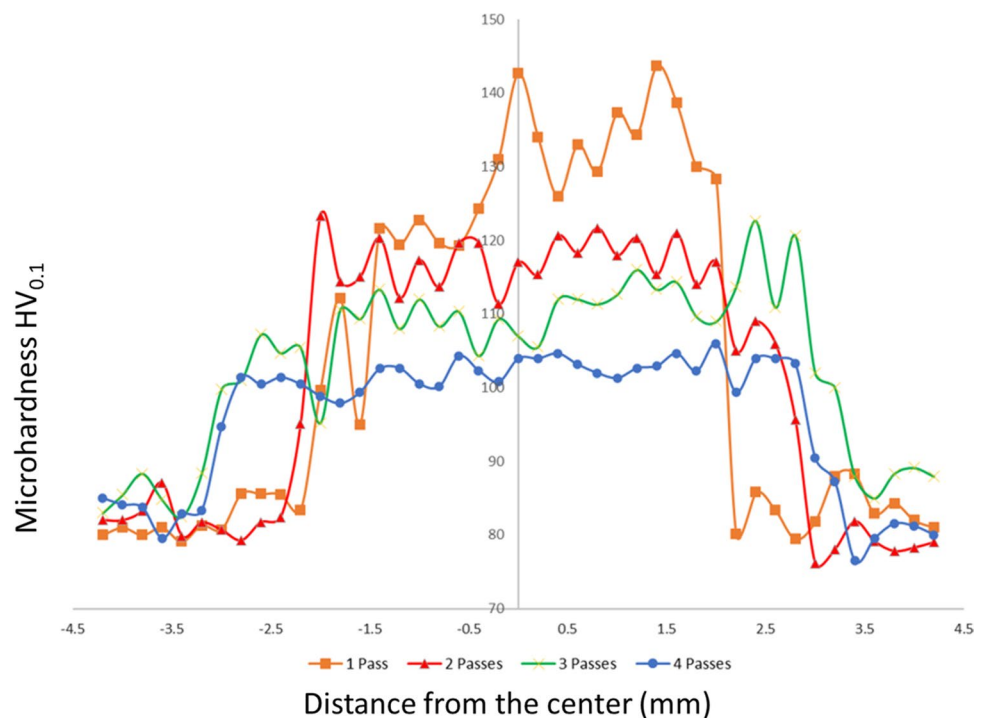
3.4 Fracture analysis

The fracture morphology was investigated using both OM and SEM to delineate the fracture pattern, as illustrated in Fig. 13. The macroscopic images in the left column, specifically Fig. 13 (a, d, g, and j), provide a comprehensive view of the FSP-processed material. Subsequent micrographs, captured via SEM, offer a more detailed analysis of fracture mechanisms. Evidently, as the number of FSP passes increases, the intensity of the dimples diminishes, transitioning the fracture from predominantly ductile characteristics to a more hybridized (ductile—brittle) nature [58]. The ductile traits seen in Fig. 13 (b, and c) suggest that the material underwent plastic deformation of a transcrystalline nature. This is typified by significant interface unevenness and a non-uniform particle distribution [59]. Such a fracture
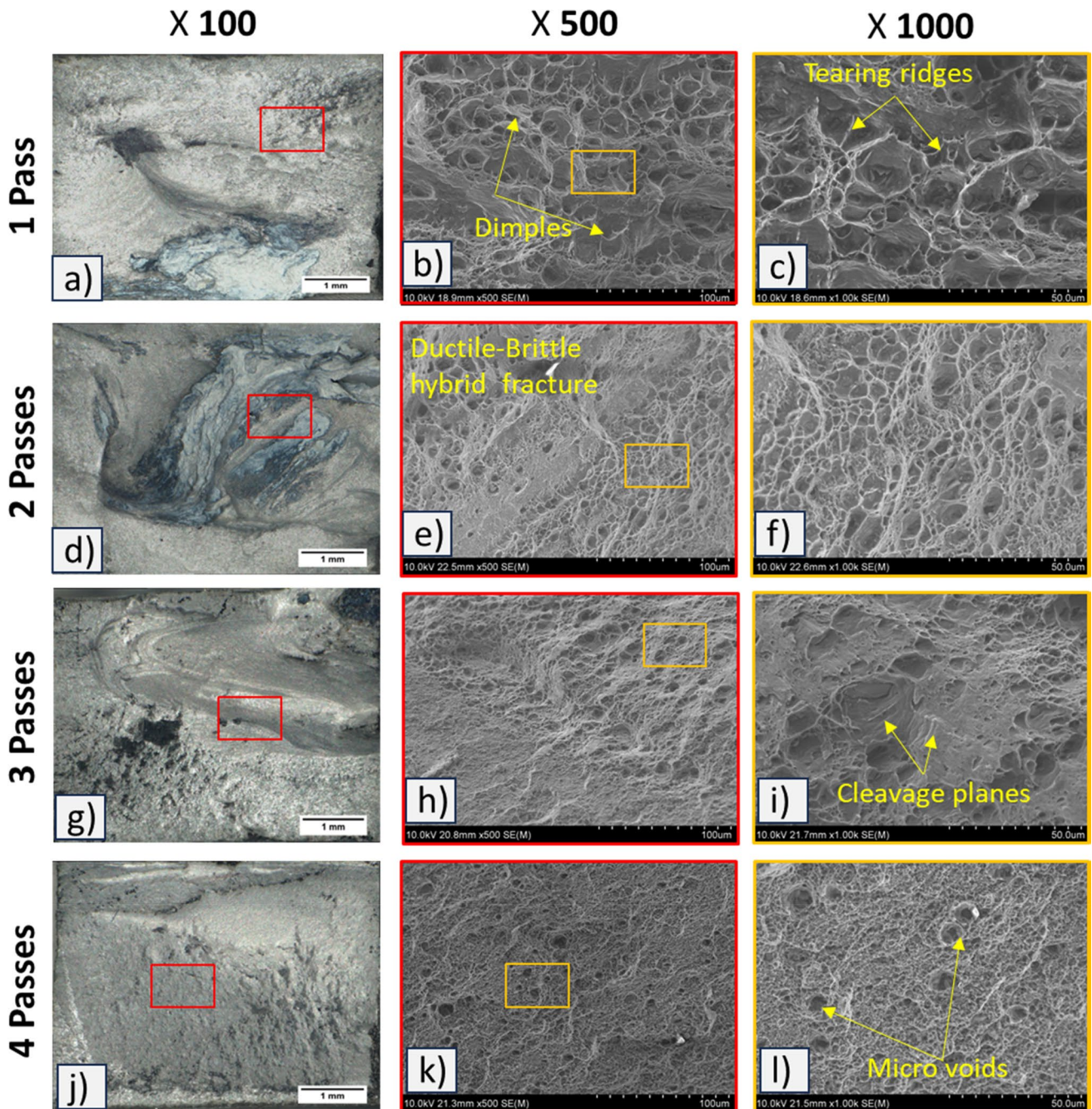

Fig. 13 Optical and SEM micrographs from fracture surfaces after 1 FSP pass (**a**, **b**,and **c**), 2 FSP passes (**d**, **e**, and **f**), 3 FSP passes (**g**, **h** and **i**), and 4 FSP passes (**j**, **i**, and **l**)

arises when the bonding strength within the aligned crystal planes exceeds the slip stress in the planes that intersect the fracture direction [60]. With an uptick in FSP passes, a mix of ductile and brittle fractures emerges. After two passes, the fracture exhibits a smoother texture, with less intense bimodal distribution of dimples. In MMCs, after a certain number of passes, regions exhibit both smaller and larger dimples (Fig. 13 e, and f)—a hallmark of well-bonded structures [61]. The pronounced dimensions of larger dimples are chiefly associated with particle-induced phenomena, while smaller dimple formations highlight the matrix's ductile fracture mechanisms [62]. Upon completing 3 FSP passes, the fracture zones (Fig. 13h) display a distinct texture, replete with elongated features indicative of significant material flow and deformation. At higher magnifications, "Cleavage planes," characteristic of brittle fractures, become discernible [63]. This implies that with an increasing number of FSP passes, certain regions within the material might be evolving toward brittleness, leading to the emergence of these cleavage planes during fractures [64]. Lastly, after four passes, the structure appears dense and complex, signifying extensive mixing and deformation. The observed features are finer, hinting at a refined grain structure or amplified material flow and amalgamation [65]. Moreover, there is a noticeable upsurge in micro-voids, likely stemming from nanoparticle agglomeration [66]. These micro-voids can act as stress concentrators, potentially reducing the overall mechanical strength of the material [67].

In general, it has been observed that the TiO_2 nanocomposites undergo a ductile–brittle fracture [68], although, as the TiO_2 consecration increases the brittle fracture progressively increase [69]. In other words, based on the number of FSP passes, the microstructure arrangement (i.e., onion-rings) and TiO_2 nanoparticle agglomeration we can observe a transitioning the fracture from predominantly ductile

characteristics to a more hybridized ductile—brittle nature. In addition, the dimple dimensions were found to be associated with their grain structure, given that grain boundaries serve as the initial sites for void nucleation [70]. The propensity for catastrophic failure escalated with the volume fraction/agglomeration of TiO_2 nanoparticles [71].

3.5 Tribological behavior

Figures 14 and 15 encapsulate the outcomes of weight loss, wear rate, coefficient of friction, and friction force over time. Meanwhile, Figs. 16, 17, 18 provide a depiction of typical post-friction surface morphologies of the examined composites.

In this tribological study, wear resistance was gaged by the weight loss of the composites. Tests were conducted under a consistent load but varied over two friction path distances: 250 m and 1000 m. The weight loss post the shorter distance test was comparable among samples, a trend that was mirrored in their wear rates. After 3 tool passes at the 250-m mark, there was a modest increase in both weight loss and wear rate; however, extending the friction path to 1000 m appeared to stabilize the process and diminish the wear rate, as illustrated in Fig. 14 a, b. This suggests that the material becomes more resistant to wear with more FSP passes and longer friction paths [72]. The enhancement of the tribological properties of the investigated composites is attributed to the homogenization of the microstructure. An increased number of FSP passes resulted in greater homogenization (Fig. 2). After three FSP passes, the characteristic "onion rings" were virtually eliminated. The uniform distribution of TiO2 particles significantly improves the tribological properties, while hardness does not influence the wear rate. The surface morphology showcased in Fig. 15 c after sliding contact with 3 Friction Stir Processing (FSP) passes
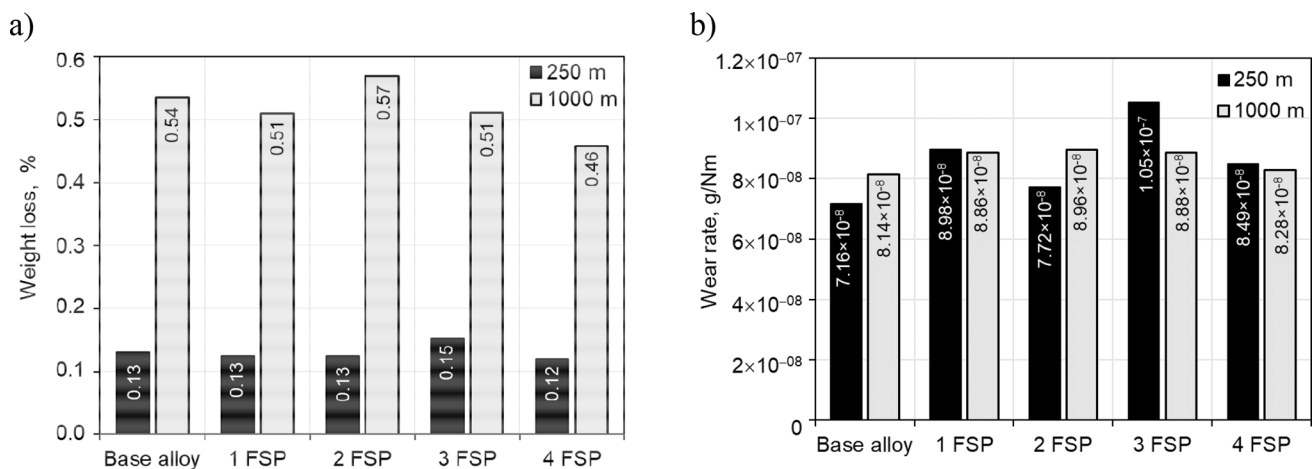

Fig. 14 Wear properties of investigated materials: **a** weight loss and **b** wear rate
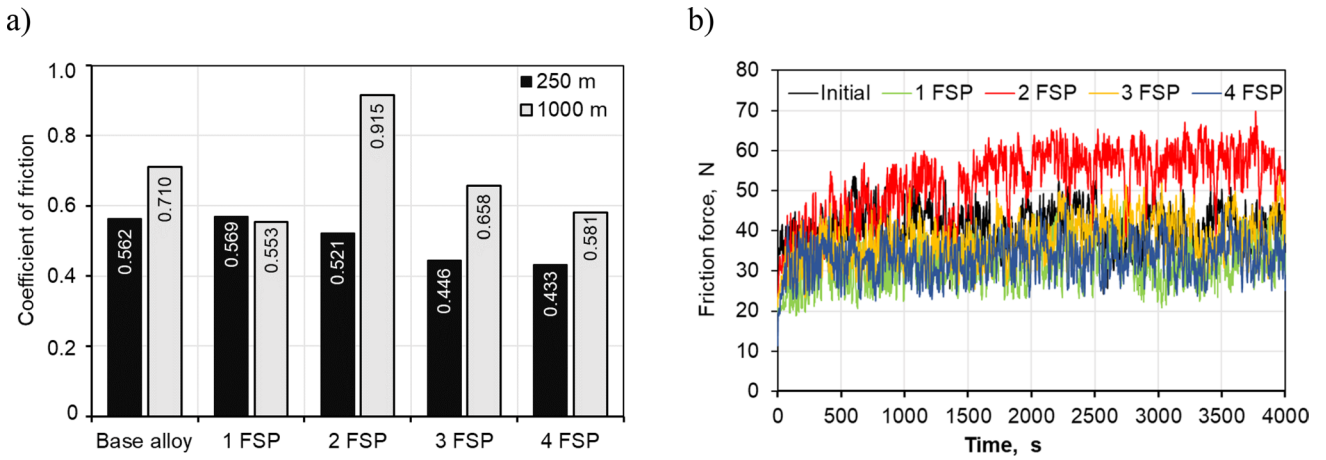
a)

b)

Fig. 15 Coefficient of friction (**a**) and friction force as a function of time (**b**)
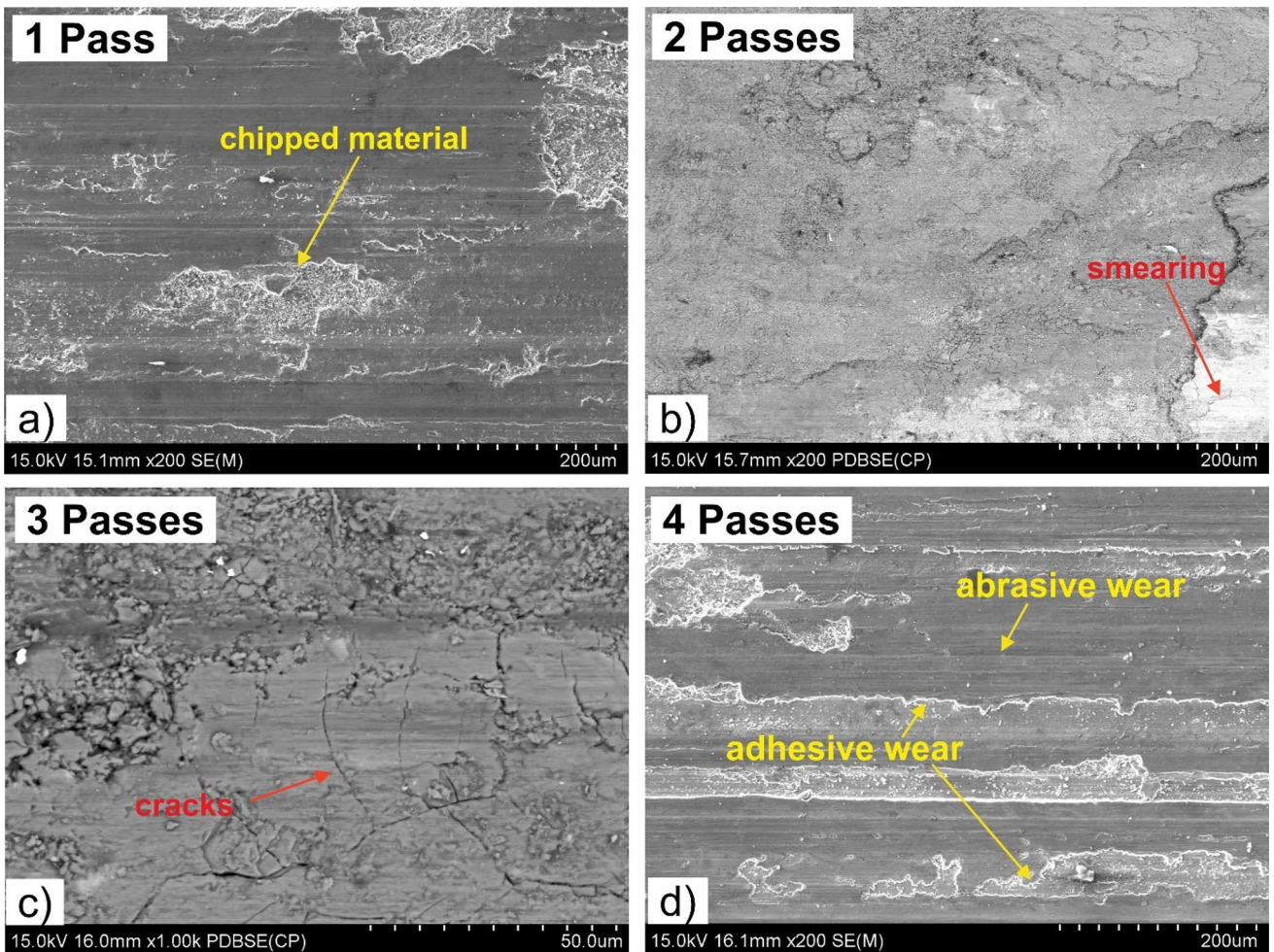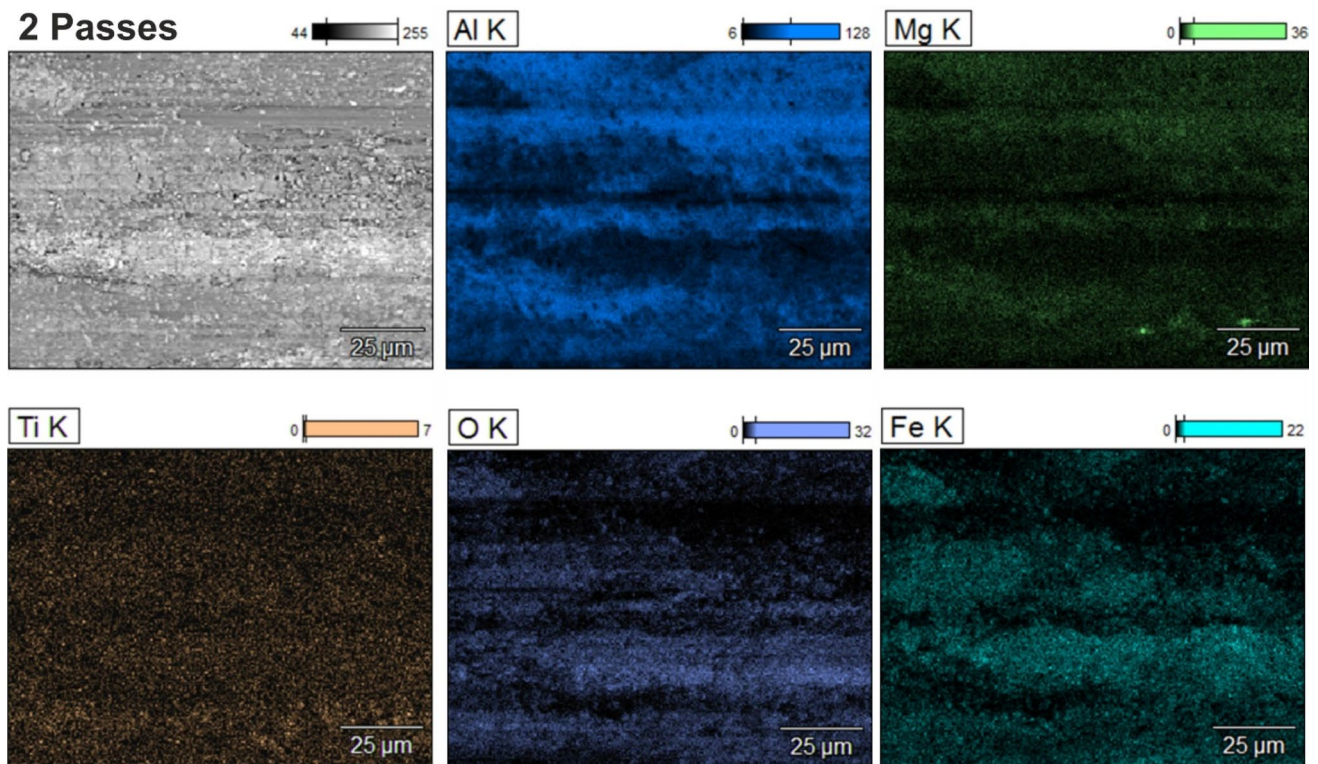

Fig. 16 Surface morphology after sliding contact under technically dry friction at a distance of 1000 m: **a** one pass, **b** two passes, **c** three passes, **d** four passes; SEM
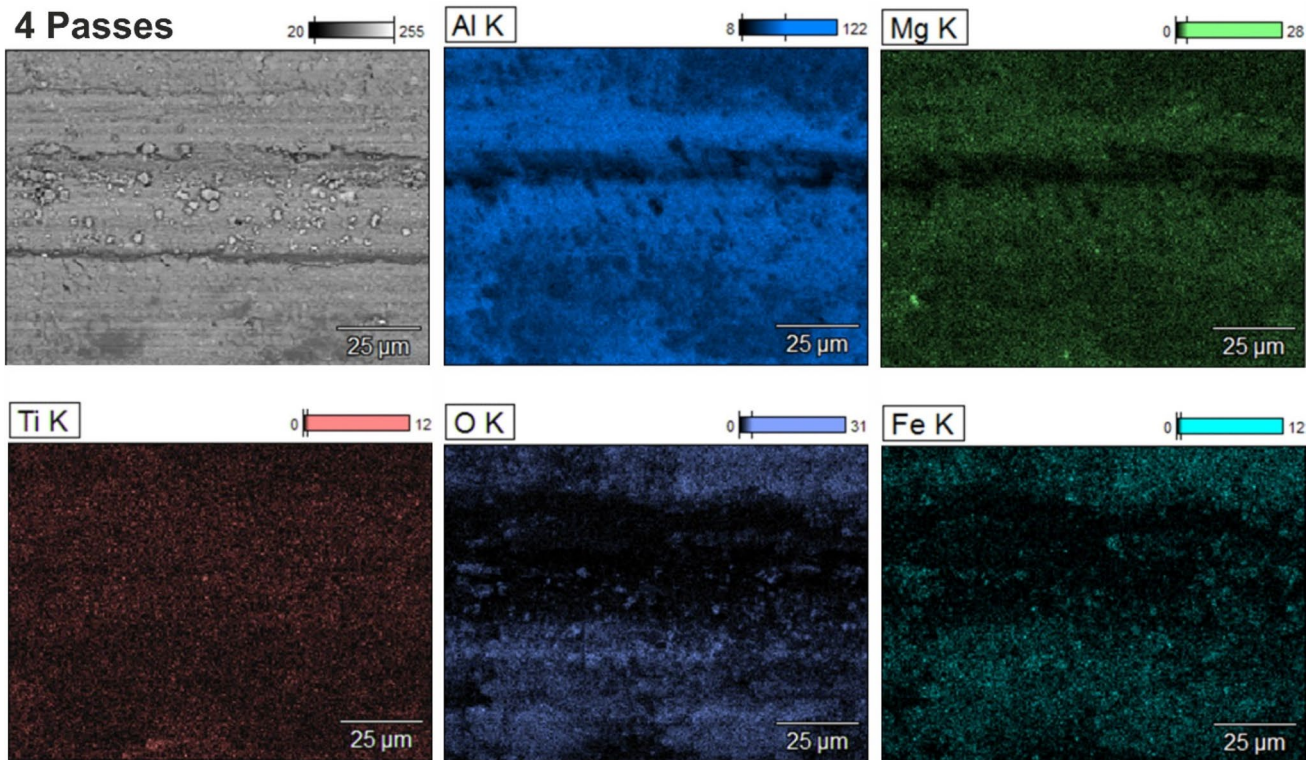
Fig. 17 Element distribution maps (Al, Mg, Ti, O, Fe) on the surface of Al-TiO$_2$ composite after two passes; friction of in dry conditions at a distance of 100 m; SEM

reveals a significant presence of fatigue cracks running perpendicular to the direction of friction. This may suggest substantial smearing of the matrix material and potentially iron from the counter sample during the initial stage of friction, which could account for the heightened wear intensity observed in the first 250 m of friction [73].

Analyzing the changes in the friction coefficient as a function of the friction distance and the number of tool passes in the FSP, it can be seen that there is a clear increase of 28.87% from the base material in the friction coefficient at a distance of 1000 m for two and more passes. The higher friction coefficient could be attributed to the particle distribution as well as the stirring zone area [74]. This phenomenon is also explained by the surface morphologies after the tribological test presented in Fig. 16 a, b, d (surfaces after friction—for 2,3,4 FSP passes). In all these materials, we observe a significant proportion of smearing, especially of the matrix material, on the contact surface, which changes the contact characteristics, facilitates the adhesion phenomenon, which translates into an increase in the friction coefficient and influences the course of friction force changes observed in the graphs (Fig. 15 b). The course of frictional force changes for the material after two FSP passes

is characterized by a significant instantaneous scatter of recorded forces and the highest values compared to the other variants tested, further confirming the increasing role of smearing. For materials after three and four passes of the tool, the coefficient of friction decreases compared to that after two passes, but remains at a higher level. This is the result of a gradual reduction in the proportion of friction node areas transferred by smearing the material. In the material after four passes (Fig. 16 d), it can be seen that the adhesion is gradually eliminated by the increased contribution of abrasive mechanisms to friction, which is confirmed by the scratches and grooves present on the surface, also observed in the sticking areas [75].

Elemental distribution maps of the surfaces post-friction were created (Figs. 17, 18), which corroborate the occurrence of iron transfer from the countersample to the tested surfaces of the aluminum matrix composites. This transfer is indicative of the materials' propensity for adhesion. In addition, oxidation has been detected within the areas where iron has adhered. It was also noted that the TiO$_2$ particles appeared fragmented and relocated into these adhesive zones, suggesting their potential role as abrasives during the friction process.

Fig. 18 Element distribution maps (Al, Mg, Ti, O, Fe) on the surface of Al-TiO$_2$ composite after four passes; friction of in dry conditions at a distance of 1000 m; SEM

Table 2 Changes in misorientation angles

Material	LABs, %	HABs, %
Base alloy	42.3	57.7
Base alloy with TiO$_2$ after FSP modification—1 FSP	5.2	94.8
Base alloy with TiO$_2$ after FSP modification—4 FSP	17.9	82.1

3.6 Summary and key findings

The following Table 2 contains all the key findings of this study in order to ensure a reproductivity of the results. The study investigates the impact of adding TiO$_2$ nanoparticles and employing multi-pass FSP on the microstructure and mechanical properties of 5083 aluminum alloy. The analysis reveals that TiO$_2$ nanoparticles, combined with multi-pass FSP, significantly refine the grain structure through mechanisms such as SPD and DRX. The refinement is further enhanced by hard nanoparticles like Al$_3$Ti and MgO, which induce PSN and restrict grain boundary migration via the Zener pinning mechanism.

Key factors contributing to the improved mechanical properties include better dispersion of nanoparticles and refined microstructure from multiple FSP passes. Enhanced uniform distribution of nanoparticles prevents agglomeration, maximizing their strengthening effects. The refined microstructure, with smaller grains and no particle agglomerates, increases material strength by hindering dislocation movement and eliminating stress concentration points. Overall, the FSP process and nanoparticle addition markedly improve the aluminum alloy's resistance to deformation and enhance its strength.

Finally, regarding the tribological properties of 5083 nanocomposites reinforced with TiO$_2$ nanoparticles through FSP, focusing on weight loss, wear rate, coefficient of friction, and friction force over time. Wear resistance was assessed under a constant load across two friction path distances: 250 and 1000 m. Initial tests showed comparable weight loss and wear rates among samples at the 250-m mark, with slight increases after three FSP passes. However, extending the friction path to 1000 m reduced the wear rate, indicating improved wear resistance with more FSP passes and longer friction paths. The homogenization of the microstructure, achieved through multiple FSP passes, plays a crucial role in enhancing the composites' tribological properties. Surface morphology analysis revealed significant fatigue cracks and matrix material smearing, contributing to increased wear intensity during initial friction. The

Table 3 Summarized Results

Variant	UTS, MPa	YS, MPa	HV0.1	Coefficient of friction 250 m/1000 m	Weight loss, % 250 m/1000 m	Wear rate, g/Nm 250 m/1000 m
AA 5083 matrix	322	142	80	0.562/0.710	0.13/0.54	$7.16 \times 10^{-8}/8.4 \times 10^{-8}$
AA 5083 matrix – TiO_2_1 FSP	232	144	137	0.569/0.553	0.13/0.51	$8.98 \times 10^{-8}/8.68 \times 10^{-8}$
AA 5083 matrix – TiO_2_2 FSP	263	152	120	0.521/0.915	0.13/0.57	$7.72 \times 10^{-8}/8.96 \times 10^{-8}$
AA 5083 matrix – TiO_2_3 FSP	322	182	111	0.446/0.658	0.15/0.51	$1.05 \times 10^{-7}/8.68 \times 10^{-8}$
AA 5083 matrix – TiO_2_4 FSP	359	192	103	0.433/0.561	0.12/0.46	$8.49 \times 10^{-8}/8.28 \times 10^{-8}$

following Table 3 contains the summarized results for the multi-pass FSP of AA5083-TiO2 nanocomposites.

It is worth mentioning that, the AA5083-TiO2 nanocomposites developed in our study show significant promise for various industrial applications. In the aerospace industry, these nanocomposites provide an advantageous blend of lightweight properties and enhanced strength, making them ideal for components requiring a high strength-to-weight ratio. Similarly, in the automotive sector, their improved wear resistance and lower friction coefficient make them valuable for high-wear parts such as pistons and gears. In addition, their corrosion resistance and superior mechanical properties render them suitable for marine applications, including structures and components exposed to harsh marine conditions. In defense, the high strength and lightweight nature of these nanocomposites make them suitable for armor plating and other robust defense components. Furthermore, the enhanced mechanical properties of these composites can boost the performance and durability of sports equipment, such as bicycle frames and golf clubs.

4 Conclusions

The present study has investigated the effects of incorporating TiO_2 nanoparticles into AA5083 MMCs using multi-pass FSP, focusing on microstructural, mechanical, and tribological properties. The experimental findings and subsequent analysis have yielded significant insights into the behavior and performance of these nanocomposites.

- Microstructural analysis revealed a significant refinement in grain size from 20 to 3 μm after one FSP pass, followed by a slight increase in the average grain size to 7 μm with subsequent passes. In addition, the size of the TiO_2 nanoparticles decreased from 220 before the FSP process to approximately 100 nm after undergoing 4 FSP passes.
- EBSD analysis revealed significant changes in crystallographic orientations and texture intensity, reflecting the transformation induced by TiO_2 incorporation during FSP. Specifically, the untreated base alloy exhibited orientations primarily along the < 101 > and < 112 > poles, with a texture intensity of 1.85. Upon the introduction of TiO_2, a single FSP pass shifted these orientations toward the < 111 > and < 110 > poles, resulting in an increased texture intensity of 2.19, which further rose to 2.86 after 4 FSP passes. In terms of misorientation angles, the base alloy had 57.7% angles larger than 15°, a percentage that surged to 95% after a single FSP pass with TiO_2 and stabilized around 82% after 4 FSP passes.
- Mechanical property assessments demonstrated notable enhancements, with the nanocomposite reaching a peak yield strength of 192 MPa and ultimate tensile strength (UTS) of 359 MPa after four FSP passes, representing a 35.2% increase in yield strength and a 11.5% increase in ultimate tensile strength compared to the base material. In addition, a steady rise in strength properties with each additional FSP pass underscored the effectiveness of the process in improving material performance.
- As the number of FSP passes increased, a noticeable decrease in microhardness was observed. Specifically, microhardness values decreased progressively from 137 HV0.1 after a single FSP pass to 120 HV0.1 after two passes, 111 HV0.1 after three passes, and 103 HV0.1 after four passes. In comparison, the base material exhibited a microhardness of approximately 80 HV0.1, with a standard deviation of 5 HV0.1. This decrease in microhardness is mainly attributed to the expanding stirring zone resulting from the more homogeneous dispersion of the nano powder throughout the composite material.
- Fracture analysis revealed a transition from purely ductile to mixed ductile—brittle fracture modes with increased FSP passes, highlighting the importance of understanding the fracture mechanisms in these nanocomposites.
- The friction coefficient decreased 22.95% and 18.16% after 4 FSP passes compared to the matrix material after 250 m and 1000 m. It seems that the addition of TiO_2 to the AA5083 aluminium alloy does not significantly affect the friction course and tribological properties of the materials tested. The dominant wear mechanisms are adhesive and abrasive wear. In addition, transfer of the countersample material to the surface of the test material was demonstrated.

Overall, the findings of this study have significant implications for the development of high-performance materials in various industrial sectors. The ability to tailor microstructural, mechanical, and tribological properties through FSP-mediated nanoparticle incorporation opens up new avenues for the design and engineering of advanced composites with enhanced strength, durability, and wear resistance. These insights contribute to the broader understanding of materials science and hold promise for applications in aerospace, automotive, marine, defense, sports equipment, where superior material properties are paramount.

Declarations

Conflict of interest Authors declare that they have no conflict of interest.

Ethical approval This article does not contain any studies with human participants or animals performed by any of the authors.

Informed consent Not applicable.

References.

1. Ozben T, Kilickap E, Çakır O. Investigation of mechanical and machinability properties of SiC particle reinforced Al-MMC. J Mater Process Technol. 2008;198(1–3):220–5.

2. Adamiak M, Fogagnolo JB, Ruiz-Navas EM, Dobrzañski LA, Torralba JM. Mechanically milled AA6061/(Ti3Al)P MMC reinforced with intermetallics – the structure and properties. J Mater Process Technol. 2004. https://doi.org/10.1016/j.jmatprotec.2004.04.202.

3. Dubourg L, Ursescu D, Hlawka F, Cornet A. Laser cladding of MMC coatings on aluminium substrate: influence of composition and microstructure on mechanical properties. Wear. 2005;258(11–12):1745–54. https://doi.org/10.1016/j.wear.2004.12.010.

4. Mathan Kumar N, Senthil Kumaran S, Kumaraswamidhas LA. An investigation of mechanical properties and corrosion resistance of Al2618 alloy reinforced with Si3N4, AlN and ZrB2 composites. J Alloys Compounds. 2015. https://doi.org/10.1016/j.jallcom.2015.08.205.

5. Jamaati R, Amirkhanlou S, Toroghinejad MR, Niroumand B. CAR process: a technique for significant enhancement of as-cast MMC properties. Mater Charact. 2011;62(12):1228–34. https://doi.org/10.1016/j.matchar.2011.10.008.

6. Singh L, Singh B, Saxena KK. Manufacturing techniques for metal matrix composites (MMC): an overview. Adv Mater Process Technol. 2020;6(2):441–57. https://doi.org/10.1080/2374068X.2020.1729603.

7. Huang G, Jie Wu, Hou W, Shen Y. Microstructure, mechanical properties and strengthening mechanism of titanium particle reinforced aluminum matrix composites produced by submerged friction stir processing. Mater Sci Eng: A. 2018. https://doi.org/10.1016/j.msea.2018.08.015.

8. Basak AK, Pramanik A, Prakash C. Deformation and strengthening of SiC reinforced Al-MMCs during in-situ micro-pillar compression. Mater Sci Eng: A. 2019. https://doi.org/10.1016/j.msea.2019.138141.

9. AshwathPazhani M, Venkatraman MA, Xavior AM, Batako A, Paulsamy J, Jayaseelan J, Anbalagan A, Bavan JS. MMC using squeeze casting method for lightweight aerospace structural applications. Mater Design. 2014. https://doi.org/10.1016/j.matdes.2023.111990.

10. Yang H, Chen X, Huang G, Song J, She J, Tan J, Zheng K, Jin Y, Jiang B, Pan F. Microstructures and mechanical properties of titanium-reinforced magnesium matrix composites: Review and perspective. J Magnesium Alloys. 2022;10(9):2311–33. https://doi.org/10.1016/j.jma.2022.07.008.

11. Ajay KP, Raj R, Kailas SV. A novel in-situ polymer derived nano ceramic MMC by friction stir processing. Mater Design. 2015. https://doi.org/10.1016/j.matdes.2015.07.054.

12. Thomas WM, Nicholas ED. Friction stir welding for the transportation industries. Mater Design. 1997;18(4–6):269–73. https://doi.org/10.1016/S0261-3069(97)00062-9.

13. Mishra RS, Ma ZY. Friction stir welding and processing. Mater Sci Eng: R: Reports. 2005;50(1–2):1–78. https://doi.org/10.1016/j.mser.2005.07.001.

14. Heidarzadeh A, Mironov S, Kaibyshev R, Çam G, Simar A, Gerlich A, Khodabakhshi F, Mostafaei A, Field DP, Robson JD, Deschamps A, Withers PJ. Friction stir welding/processing of metals and alloys: a comprehensive review on microstructural evolution. Progress Mater Sci. 2021. https://doi.org/10.1016/j.pmatsci.2020.100752.

15. Yousefpour F, Jamaati R, Aval HJ. Investigation of microstructure, crystallographic texture and mechanical behavior of magnesium-based nanocomposite fabricated via multi-pass FSP for biomedical applications. J Mech Behavior Biomed Mater. 2022. https://doi.org/10.1016/j.jmbbm.2021.104894.

16. Jiang J, Jiang F, Zhang M, Yi K. Microstructure evolution and tensile property of deformed Al–Mg–Sc alloy: comparison of ECAP and FSP. J Mater Res Technol. 2023. https://doi.org/10.1016/j.jmrt.2022.12.109.

17. Xue P, Xiao BL, Ma ZY. Enhanced strength and ductility of friction stir processed Cu–Al alloys with abundant twin boundaries. Scripta Mater. 2013;68(9):751–4. https://doi.org/10.1016/j.scriptamat.2013.01.003.

18. Sadeghi B, Shamanian M, Ashrafizadeh F, Cavaliere P, Rizzo A. Friction stir processing of spark plasma sintered aluminum matrix composites with bimodal micro- and nano-sized reinforcing Al2O3 particles. J Manufactur Processes. 2018. https://doi.org/10.1016/j.jmapro.2018.03.013.

19. Lee IS, Kao PW, Ho NJ. Microstructure and mechanical properties of Al–Fe in situ nanocomposite produced by friction stir processing. Intermetallics. 2008;16(9):1104–8. https://doi.org/10.1016/j.intermet.2008.06.017.

20. Ke L, Huang C, Xing L, Huang K. Al–Ni intermetallic composites produced in situ by friction stir processing. J Alloys Compounds. 2010;503(2):494–9. https://doi.org/10.1016/j.jallcom.2010.05.040.

21. Lee IS, Kao PW, Chang CP, Ho NJ. Formation of Al–Mo inter-metallic particle-strengthened aluminum alloys by friction stir processing. Intermetallics. 2013. https://doi.org/10.1016/j.intermet.2012.11.018.

22. Hsu CJ, Kao PW, Ho NJ. Intermetallic-reinforced aluminum matrix composites produced in situ by friction stir processing. Mater Lett. 2007;61(6):1315–8. https://doi.org/10.1016/j.matlet.2006.07.021.

23. Wang W, Shi Q-y, Liu P, Li H-k, Li T. A novel way to produce bulk SiCp reinforced aluminum metal matrix composites by friction stir processing. J Mater Process Technol. 2009;209(4):2099–103. https://doi.org/10.1016/j.jmatprotec.2008.05.001.

24. Devaraju A, Kumar A, Kumaraswamy A, Kotiveerachari B. Influence of reinforcements (SiC and Al2O3) and rotational speed on wear and mechanical properties of aluminum alloy 6061–T6 based surface hybrid composites produced via friction stir processing. Mater Design. 2013. https://doi.org/10.1016/j.matdes.2013.04.029.

25. Arora HS, Singh H, Dhindaw BK. Composite fabrication using friction stir processing—a review. Int J Adv Manuf Technol. 2012;61:1043–55. https://doi.org/10.1007/s00170-011-3758-8.

26. Derazkola HA, Simchi A. Processing and characterizations of polycarbonate/alumina nanocomposites by additive powder fed friction stir processing. Thin-Walled Struct. 2020. https://doi.org/10.1016/j.tws.2020.107086.

27. Maji P, Nath RK, Pritam Paul RK, Meitei B, Ghosh SK. Effect of processing speed on wear and corrosion behavior of novel MoS2 and CeO2 reinforced hybrid aluminum matrix composites fabricated by friction stir processing. J Manufact Processes. 2021. https://doi.org/10.1016/j.jmapro.2021.07.032.

28. Papantoniou IG, Kyriakopoulou HP, Pantelis DI, et al. Manufacturing process of AA5083/nano-γAl2O3 localized composite metal foam fabricated by friction stir processing route (FSP) and microstructural characterization. J Mater Sci. 2018;53:3817–35. https://doi.org/10.1007/s10853-017-1802-2.

29. Orłowska M, Pixner F, Hütter A, Enzinger N, Olejnik L, Lewandowska M. Manufacturing of coarse and ultrafine-grained aluminum matrix composites reinforced with Al2O3 nanoparticles via friction stir processing. J Manufact Processes. 2022. https://doi.org/10.1016/j.jmapro.2022.06.011.

30. Ostovan F, Azimifar I, Toozandehjani M, Shafiei E, Shamshirsaz M. Synthesis of ex-situ Al5083 reinforced with mechanically-alloyed CNTs and Fe2O3 nanoparticles using friction stir processing. J Mater Res Technol. 2021. https://doi.org/10.1016/j.jmrt.2021.07.072.

31. Li X, Zhang Z, Peng Y, Yan D, Tan Z, Zhou Qi, Wang K. In situ synthesized nano-Al4C3 reinforced aluminum matrix composites via friction stir processing. J Mater Res Technol. 2021. https://doi.org/10.1016/j.jmrt.2021.07.109.

32. Ata MH, Abdel-Gaber GT, Elkady O, Fathy M, Abu-Okail M. An Investigation on microstructural and mechanical properties of an innovative hybrid AA1050/Ni-Cu-Fe via mechanical alloying and friction stir processing. CIRP J Manufact Sci Technol. 2022. https://doi.org/10.1016/j.cirpj.2022.10.001.

33. Chittoriya BS, Jayant A, Kumar R. Effect of Multipass FSP and (SiC + TiB2) nanoparticles on the mechanical and metallurgical characteristic of the hybrid metal matrix composite. SILICON. 2023;15:7927–41. https://doi.org/10.1007/s12633-023-02635-9.

34. Mohammed MM, Abdullah ME, Rohim MNM, Kubit A, Aghajani DH. AA5754–Al2O3 nanocomposite prepared by friction stir processing: microstructural evolution and mechanical performance. J Manufact Mater Process. 2024;8(2):58. https://doi.org/10.3390/jmmp8020058.

35. Heidarzadeh A, Khajeh R, Jafarian HR, Tutunchi A, Ahmed M, Lee J, Park N. A pathway towards strengthening and ductilization of additive-manufactured AlSi10Mg through friction stir processing: Microstructural evolution and tensile behavior. Mater Sci Eng: A. 2024. https://doi.org/10.1016/j.msea.2024.146367.

36. Zhang C, Bai J, Sun Y, Xiu W. Effect of friction stir processing on grain orientation evolution and coincidence site lattice boundaries of Al6061. Mater Lett. 2024. https://doi.org/10.1016/j.matlet.2023.135326.

37. Xin-wei SHE, Xian-quan J, Pu-quan W, Bin-bin T, Kang C, Yu-jie L, Wei-nan C. Relationship between microstructure and mechanical properties of 5083 aluminum alloy thick plate. Trans Nonferrous Metals Society China. 2020;30(7):1780–9. https://doi.org/10.1016/S1003-6326(20)65338-9.

38. Xia SL, Ma M, Zhang JX, Wang WX, Liu WC. Effect of heating rate on the microstructure, texture and tensile properties of continuous cast AA 5083 aluminum alloy. Mater Sci Eng: A. 2014;609:168–76. https://doi.org/10.1016/j.msea.2014.05.002.

39. García-Bernal MA, Mishra RS, Verma R, Hernández-Silva D. Influence of friction stir processing tool design on microstructure and superplastic behavior of Al-Mg alloys. Mater Sci Eng: A. 2016;670:9–16. https://doi.org/10.1016/j.msea.2016.05.115.

40. R. S. Mishra, P. S. De i N. Kumar, Friction Stir Welding and Processing, Science and Engineering, Switzerland: Springer International Publishing, 2014

41. Hamilton C, Kopyściański M, Senkovi O, Dymek S. A coupled thermal/material flow model of friction stir welding. Metallurgical Mater Trans A. 2013;44A:1730–40.

42. Hamilton C, Węglowskii MS, Dymek S. A simulation of friction-stir processing for temperature and material flow". Metallurgical Mater Trans B. 2015;46B:1409–18.

43. Ma ZY. Friction stir processing technology: a review. METALLURGICAL MATER TRANS A tom. 2008;39A:642–58.

44. Węglowski MS. Friction stir processing – State of the art. Archives Civil Mechanical Eng tom. 2018;18:114–29.

45. Heidarzadeh A, Mironov S, Kaibyshev R, Çam G, Simar A, Gerlich A, Khodabakhshi F, Mostafaei A, Field DP, Robson JD, Deschampsi A, Withers PJ. Friction stir welding/processing of metals and alloys: a comprehensive review on microstructural evolution". Progress Mater Sci. 2020. https://doi.org/10.1016/j.pmatsci.2020.100752.

46. Sun T, Cao F, Hu J, et al. Developing ultrafine twinned microstructure enabled excellent strength-ductility synergy in Mg–Al–Zn alloy by submerged friction stir processing. Metall Mater Trans A. 2023;54:4779–95. https://doi.org/10.1007/s11661-023-07201-x.

47. Jha KK, Kesharwani R, Imam M. Microstructure, texture, and mechanical properties correlation of AA5083/AA6061/SiC composite fabricated by FSAM process. Mater Chem Physics. 2023. https://doi.org/10.1016/j.matchemphys.2022.127210.

48 Khodabakhshi F, Simchi A, Kokabi AH, Gerlich AP, Nosko M. Effects of post-annealing on the microstructure and mechanical properties of friction stir processed Al–Mg–TiO2 nanocomposites. Mater Design. 2014;63:30–41. https://doi.org/10.1016/j.matdes.2014.05.065.

49. Khodabakhshi F, Simchi A, Kokabi A, et al. Strain rate sensitivity, work hardening, and fracture behavior of an Al-Mg TiO2Nanocomposite prepared by friction stir processing. Metall Mater Trans. 2014;A45:4073–88. https://doi.org/10.1007/s11661-014-2330-1.

50. Khodabakhshi F, Simchi A, Kokabi AH, Gerlich AP, Nosko M. Effects of post-annealing on the microstructure and mechanical properties of friction stir processed Al–Mg–TiO2 nanocomposites. Mater Des. 2014;63:30–41. https://doi.org/10.1016/j.matdes.2014.05.065.

51. Husain Mehdi RS, Mishra,. Effect of multi-pass friction stir processing and SiC nanoparticles on microstructure and mechanical properties of AA6082-T6. Adv Industrial Manufact Eng. 2021. https://doi.org/10.1016/j.aime.2021.100062.

52. Hashmi AW, Mehdi H, Mishra RS, et al. Mechanical properties and microstructure evolution of AA6082/Sic nanocomposite processed by multi-pass FSP. Trans Indian Inst Met. 2022;75:2077–90. https://doi.org/10.1007/s12666-022-02582-w.

53. SivaneshPrabhu M, ElayaPerumal A, Arulvel S. Development of multi-pass processed AA6082/SiCp surface composite using friction stir processing and its mechanical and tribology characterization. Surface Coat Technol. 2020. https://doi.org/10.1016/j.surfcoat.2020.125900.

54. Khodabakhshi F, Simchi A, Kokabi A, et al. Strain rate sensitivity, work hardening, and fracture behavior of an Al-Mg TiO2 nanocomposite prepared by friction stir processing. Metall Mater Trans A. 2014;45:4073–88. https://doi.org/10.1007/s11661-014-2330-1.

55. Girish G, Anandakrishnan V. Fabrication of Al-Zn-Mg-Cu matrix composite by multi-pass recursive friction stir processing and its characterization. J Materi Eng Perform. 2021;30:5868–88. https://doi.org/10.1007/s11665-021-05844-8.

56. Bahrami M, Dehghani K, Givi MKB. A novel approach to develop aluminum matrix nano-composite employing friction stir welding technique. Mater Design. 2014;53:217–25. https://doi.org/10.1016/j.matdes.2013.07.006.

57. Mirjavadi SS, Alipour M, SoheilEmamian S, Kord AMSH, Koppad PG, Keshavamurthy R. Influence of TiO2 nanoparticles incorporation to friction stir welded 5083 aluminum alloy on the microstructure mechanical properties and wear resistance. J Alloys Compd. 2017;712:795–803. https://doi.org/10.1016/j.jallcom.2017.04.114.

58. Han R, Ren D, Zhang Z, et al. Study on improving the formability of AA6061-T6 alloy by surface FSP. Int J Adv Manuf Technol. 2023;128:1815–27. https://doi.org/10.1007/s00170-023-12033-5.

59. SarkariKhorrami M, Kazeminezhad M, Kokabi AH. The effect of SiC nanoparticles on the friction stir processing of severely deformed aluminum. Mater Sci Eng: A. 2014;602:110–8. https://doi.org/10.1016/j.msea.2014.02.067.

60. French IE, Weestrich PF. The shear mode of ductile fracture in materials with few inclusions. Metall Trans A. 1976;7:1841–5. https://doi.org/10.1007/BF02659814.

61. Bauri R, Devinder Yadav CN, Shyam Kumar B, Balaji,. Tungsten particle reinforced Al 5083 composite with high strength and ductility. Mater Sci Eng: A. 2015;620:67–75. https://doi.org/10.1016/j.msea.2014.09.108.

62. Wang H, Zhang H, Cui Z, Chen Z, Chen D, Wang H. Investigation on the high-temperature ductility and fracture mechanisms of an in-situ particle reinforced Al matrix composite 7075Al/TiB2. Mater Sci Eng: A. 2019. https://doi.org/10.1016/j.msea.2019.138263.

63. Petch NJ. The cleavage strength of polycrystals. J Iron Steel Inst. 1953;174:25–8.

64. Rao AG, Deshmukh VP, Prabhu N, Kashyap BP. Ductilizing of a brittle as-cast hypereutectic Al–Si alloy by friction stir processing. Mater Lett. 2015;159:417–9. https://doi.org/10.1016/j.matlet.2015.07.006.

65. Nourbakhsh SH, Tavakoli M, Shahrokhian A. Investigations of mechanical, microstructural and tribological properties of Al2024 nanocomposite reinforced by TiO2 nanoparticles. Mater Res Express. 2018. https://doi.org/10.1088/2053-1591/aaded1.

66. Bharat N, Bose PSC. Effect of TiO2 and SiC nanoparticles on the microstructure and mechanical characteristics of AA7178 metal matrix composite. Inter Metalcast. 2023;17:2849–61. https://doi.org/10.1007/s40962-023-00959-1.

67. Shin J, Choi H, Cho M, Bae D. Effect of the interface layer on the mechanical behavior of TiO2 nanoparticle reinforced aluminum matrix composites. J Compos Mater. 2014;48(1):99–106. https://doi.org/10.1177/0021998312469238.

68. Khodabakhshi F, Simchi A, Kokabi AH, Nosko M, Simanĉik F, Švec P. Microstructure and texture development during friction stir processing of Al–Mg alloy sheets with TiO2 nanoparticles. Mater Sci Eng: A. 2014;605:108–18. https://doi.org/10.1016/j.msea.2014.03.008.

69. Liu Q, Ke L, Liu F, Huang C, Xing Li. Microstructure and mechanical property of multi-walled carbon nanotubes reinforced aluminum matrix composites fabricated by friction stir processing. Mater Design. 2013;45:343–8. https://doi.org/10.1016/j.matdes.2012.08.036.

70. SahandiZangabad P, Khodabakhshi F, Simchi A, Kokabi AH. Fatigue fracture of friction-stir processed Al–Al3Ti–MgO hybrid nanocomposites. Int J Fatigue. 2016;87:266–78. https://doi.org/10.1016/j.ijfatigue.2016.02.007.

71. AbuShanab WS, Moustafa EB. Effects of friction stir processing parameters on the wear resistance and mechanical properties of fabricated metal matrix nanocomposites (MMNCs) surface. J Mater Res Technol. 2020;9(4):7460–71. https://doi.org/10.1016/j.jmrt.2020.04.073.

72. Sharma A, Fujii H, Paul J. Influence of reinforcement incorporation approach on mechanical and tribological properties of AA6061- CNT nanocomposite fabricated via FSP. J Manufact Processes. 2020;59:604–20. https://doi.org/10.1016/j.jmapro.2020.10.016.

73. Sharma A, Narsimhachary D, Sharma VM, Sahoo B, Paul J. Surface modification of Al6061-SiC surface composite through impregnation of graphene, graphite & carbon nanotubes via FSP: a tribological study. Surface Coat Technol. 2019;368:175–91. https://doi.org/10.1016/j.surfcoat.2019.04.001.

74. Barmouz M, Givi MKB. Fabrication of in situ Cu/SiC composites using multi-pass friction stir processing: evaluation of microstructural, porosity, mechanical and electrical behavior. Composites Part A: App Sci Manufact. 2011;42(10):1445–53. https://doi.org/10.1016/j.compositesa.2011.06.010.

75. Huang G, Hou W, Li J, Shen Y. Development of surface composite based on Al-Cu system by friction stir processing: evaluation of microstructure, formation mechanism and wear behavior. Surface Coat Technol. 2018;344:30–42. https://doi.org/10.1016/j.surfcoat.2018.03.005.